Doctoral Dissertation (Censored)
博士論文（要約）

Bisphenanthroline Macrocyclic Scaffolds for Anisotropic Metallonanofibers and Chiral Heterodinuclear $Pt^{II}Cu^{I}$ Complexes

（ビスフェナントロリン大環状分子を基盤とした異方性金属ナノファイバーおよびキラルなヘテロ二核 $Pt^{II}Cu^{I}$ 錯体の構築）

A Dissertation Submitted for the Degree of Doctor of Philosophy
December 2020
令和 2 年 12 月博士（理学）申請

Department of Chemistry, Graduate School of Science,
The University of Tokyo
東京大学大学院理学系研究科
化学専攻

Shun Shimizu
清水　駿

Abstract

1. General introduction

Arrangement of metal ions is the essential factor for properties and functions of natural and artificial multinuclear metal complexes. In this context, macrocyclic molecules are fascinating structural motifs in supramolecular chemistry and materials science today because of the advantages of their well-defined cavities for precise molecular arrangement and the resulting metal-surrounded confined space for unique molecular recognition and reaction fields. In general, such macrocycles are highly symmetric, and therefore their properties and self-assembling structures tend to be non-directional or isotropic. On the other hand, from the viewpoint of metal-based functional materials such as electrical nanowires and asymmetric catalysts, it is necessary to establish a general method for inducing anisotropy or asymmetricity in macrocyclic metal complexes.

Our group has previously reported a bisphenanthroline macrocycle with two inward phenanthroline moieties for entrapping two metal ions in the rigid macrocyclic cavity. By utilizing the two coordination sites, a series of homometallic or heterometallic dinuclear complexes have been synthesized in thermodynamic control. For instance, the homodinuclear Ag^{I} complex was prepared to show its guest-specific molecular recognition ability,[1] and the homodinuclear Pd^{II} complexes were found to one-dimensionally self-assemble into Pd^{II}-assembled nanofibers.[2] However, the applicable metal ions were limited especially in the case of heterometallic and one-dimensional arrangement.

The purpose of this study was to develop a methodology for anisotropic or asymmetric arrangement of metal ions by fully utilizing the bisphenanthroline macrocycles. Here I report three systems: protonation-induced one-dimensional assembly of macrocycles arranged with metal ions, kinetically-controlled syntheses of macrocyclic heterodinuclear metal complexes, and arrangement of two different metal ions with chirality at both metal centers (Figure 1).

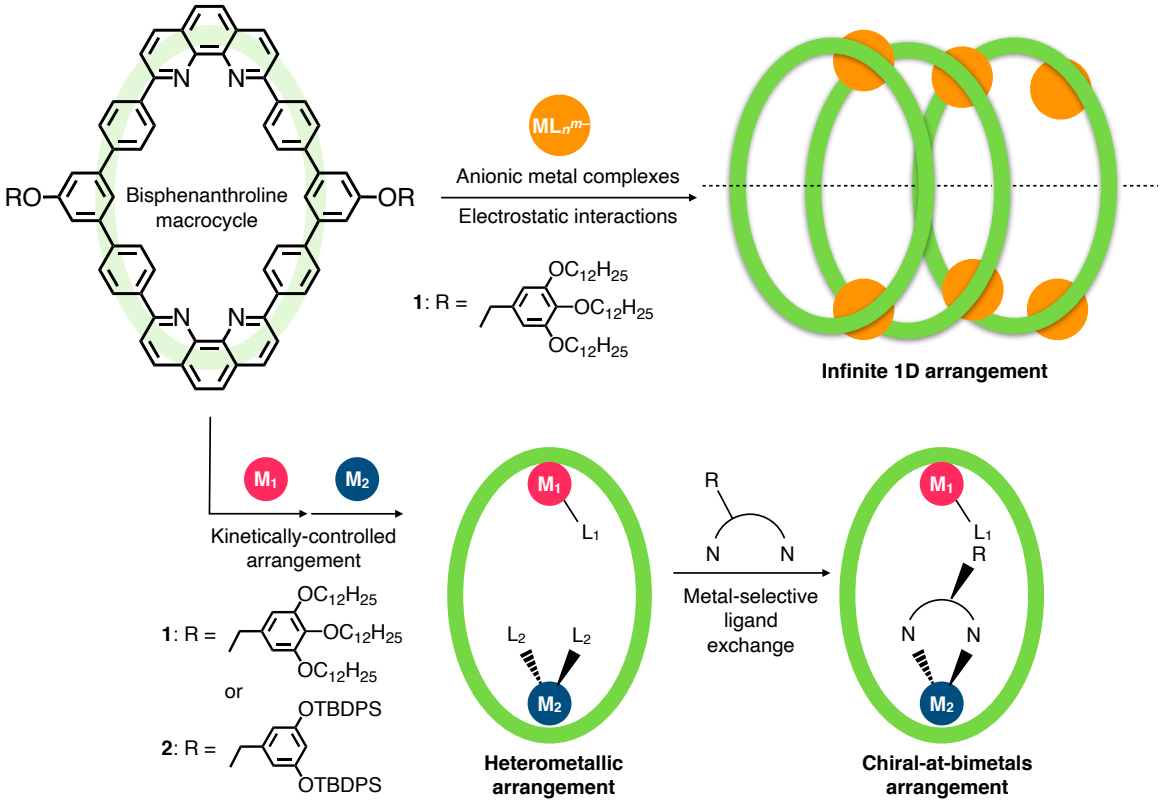

Figure 1. Outline of this research: infinite one-dimensional arrangement of anionic metal complexes, kinetically-controlled synthesis of heterodinuclear metal complexes, and construction of chiral-at-bimetals heterodinuclear complexes.

2. Protonation-induced self-assembly of bisphenanthroline macrocycles into metal-assembled nanofibers

Metal-assembled nanofibers were constructed by mixing bisphenanthroline macrocycle **1** and protic acids of anionic metal complexes. Studies on Au^{III}-assembled nanofibers composed of **1** and $HAuCl_4$ revealed that two phenanthroline moieties of **1** are protonated, and electrostatic interaction between the protonated **1** and $AuCl_4^-$ is the driving force for one-dimensional self-assembly (Fig. 2a). Their fiber structure and the alignment of Au^{III} ions along it were confirmed by the STEM-EDS analysis (Fig. 2b,c). The protonation-induced assembly was further applied to other metal-containing anions with different sizes and charge numbers, such as H_2PtCl_6 and $H_3PMo_{12}O_{40}$ as observed by STEM-EDS analyses (Fig. 2d-g). Since the nanofibers were expected to exhibit properties derived from accumulated metal ions, chemical reduction was conducted as an application of the nanofibers. For instance, the accumulated Au^{III} ions could be chemically reduced by $NaBH_4$ to Au nanoparticles with a relatively controlled size and dispersibility in organic solvents (Fig. 3a,b). On the other hand, the Mo^{VI}-assembled nanofibers could be partially reduced by L-ascorbic to afford Mo^{VI}/Mo^{V} mixed-valence nanofibers. Their chemical state and fiber structures were confirmed by UV-vis spectroscopy and AFM measurements, respectively (Fig. 3c,d). These results suggest that the protonation-induced assembly method can be applied to various metal ions regardless of their coordination geometries, and the accumulated metal ions can show array-specific reduced states.

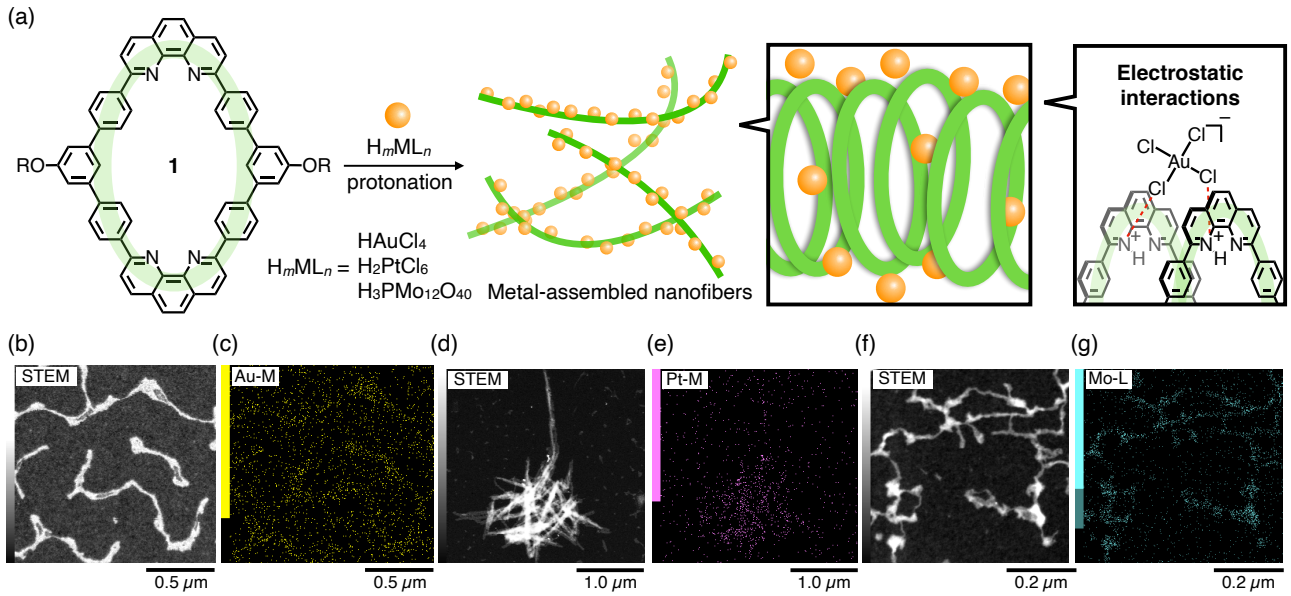

Figure 2. Protonation-induced one-dimensional assembly of **1** arrayed with metal ions: (a) schematic representation of the fiber formation; (b,c) a dark-field STEM image and an EDS-map for Au (M-peak) of the Au^{III}-assembled nanofibers; (d,e) a dark-field STEM image and an EDS-map for Pt (M-peak) of the Pt^{IV}-assembled nanofibers; (f,g) a dark-field STEM image and an EDS-map for Mo (L-peak) of the Mo^{VI}-assembled nanofibers.

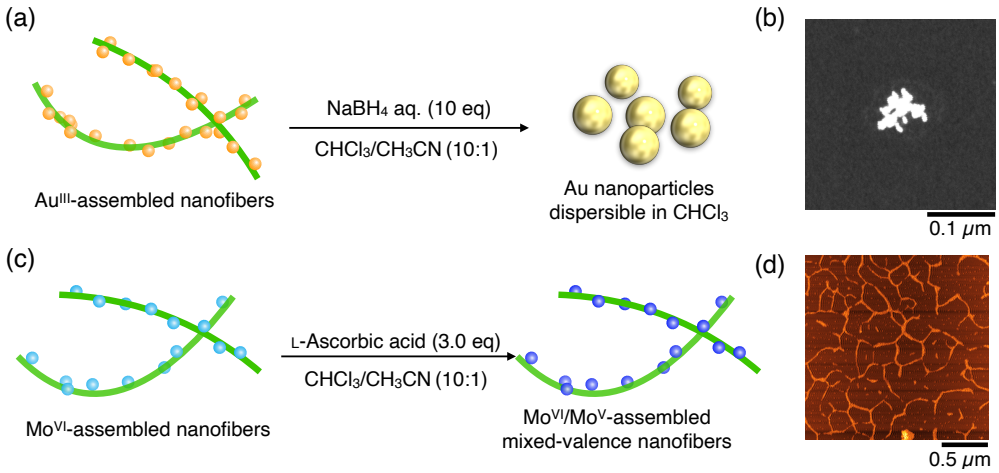

Figure 3. Reduction of metal-assembled nanofibers: (a) reduction of Au^{III}-assembled nanofibers into Au nanoparticles; (b) a dark-field STEM image of the nanoparticles; (c) reduction of Mo^{VI}-assembled nanofibers into Mo^{VI}/Mo^{V} mixed-valence nanofibers.

3. Kinetically controlled synthesis of bisphenanthroline macrocyclic heterodinuclear metal complexes

The bisphenanthroline macrocyclic ligands have been widely studied as a platform for the placement of two homogeneous metal ions, but precise synthesis of heterogeneous dinuclear metal complexes remains unexplored.[3] From this viewpoint, a mononuclear Pt^{II} complex was an attractive scaffold because the kinetically stable nature of the cyclometalated Pt^{II} center was expected to allow coordination at the vacant phenanthroline site without undergoing transmetalation (Fig. 4a). A mononuclear Pt^{II} complex of bisphenanthroline macrocyclic ligand was prepared by reaction with $PtCl_2(dmso)_2$ and repetitive column chromatography to separate the dinuclear Pt^{II} complexes. The binding behavior of the mononuclear [PtCl(H_{-1}**1**)] complex to metal ions was examined by titration experiments using Zn^{II} or Cu^{I} sources monitored by ^{1}H NMR spectroscopy, UV-vis spectroscopy, and ESI-MS spectrometry. In particular, it was revealed that addition of equimolar amount of $[Cu(CH_3CN)_4](BF_4)$ in $CHCl_3/CH_3CN$ (9:1) smoothly afforded a $Pt^{II}Cu^{I}$ heterodinuclear complex, while signals spread indicating fast ligand exchange around the Cu^{I} center. Therefore, the heterodinuclear structure was stabilized by the second bidentate ligands. ^{1}H NMR spectroscopy and ESI-TOF MS spectrometry showed that 1,10-phenanthroline derivatives with phenyl substituents at the α-position of the nitrogen atoms, 2,9-diphenyl-1,10-phenanthroline (dpp), could serve as stabilizer of the Cu^{I} center against both ligand exchange and oxidation to Cu^{II} by molecular oxygen to yield the desired heterodinuclear $Pt^{II}Cu^{I}$ complex [PtCuCl(H_{-1}**1**)(dpp)](BF_4) that is stable in air for several weeks as confirmed by ^{1}H NMR spectroscopy (Fig. 4b) and ESI-TOF MS spectrometry (m/z = 2756.534 for [PtCuCl(H_{-1}**1**)(dpp)]$^+$).

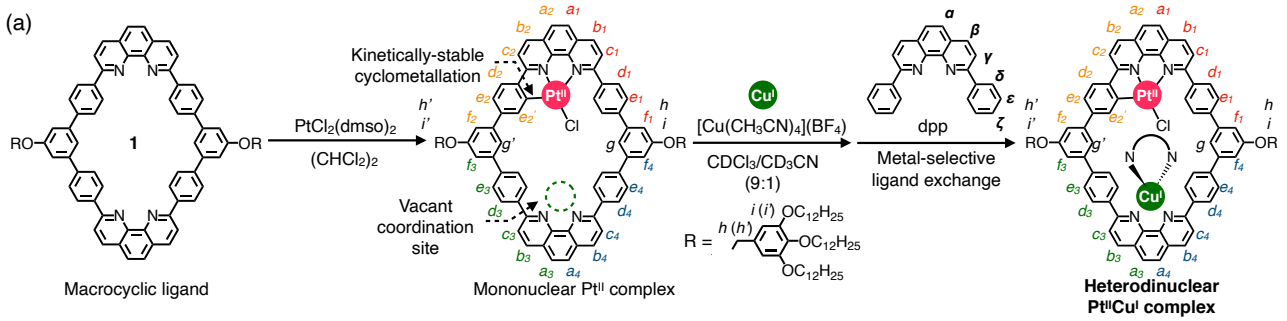

Figure 4. The kinetically controlled synthesis of macrocyclic heterodinuclear complexes: (a) Synthetic scheme of macrocyclic heterodinuclear $Pt^{II}Cu^{I}$ complexes; (b) ^{1}H NMR spectrum (500 MHz, 300 K, $CDCl_3/CD_3CN$ = 9:1) for (1) [PtCl(H_{-1}**1**)], (2) [PtCuCl(H_{-1}**1**)$(X)_2$](X) (X = Cl, CH_3CN or CD_3CN) and (3) [PtCuCl(H_{-1}**1**)(dpp)](BF_4).

4. Diastereoselective synthesis of chiral-at-bimetal heterodinuclear $Pt^{II}Cu^{I}$ complexes

The less symmetrical $Pt^{II}Cu^{I}$ complexes could be further applied to the synthesis of chiral-at-bimetals complexes by asymmetrically placing only achiral ligands. In other words, the effect of asymmetric induction at the tetrahedral Cu^{I} center on the square-planar Pt^{II} center was investigated to diastereoselectively synthesize chiral-at-bimetals heterodinuclear $Pt^{II}Cu^{I}$ complexes (Fig. 5a). For this purpose, a C_S symmetrical derivative of the dpp ligand with a phenyl group at the 5-position, 5-Ph-dpp, was introduced to the C_S symmetrical heterodinuclear $Pt^{II}Cu^{I}$ complex of a bisphenanthroline macrocyclic ligand **2** with bulky side chains. The metal-selective ligand exchange reaction could be carried out by adding 1.0 eq of 5-Ph-dpp as a secondary ligand, resulting in the complicated ^{1}H NMR signals of the chiral-at-bimetals heterodinuclear [PtCuCl(H_{-1}**2**)(5-Ph-dpp)](BF_4) complex. Furthermore, the crystal structure of this complex not only showed chirality at the distorted tetrahedral Cu^{I} center, but also at the distorted square-planar Pt^{II} center, indicating diastereoselective formation of $(R)_{Cu}(S)_{Pt}$-/$(S)_{Cu}(R)_{Pt}$-[PtCuCl(H_{-1}**2**)(5-Ph-dpp)](BF_4). This unprecedented diastereoselectivity could be attributed to the low stability of the opposite $(R)_{Cu}(R)_{Pt}$-/$(S)_{Cu}(S)_{Pt}$-isomers due to the steric hindrance between the bulky 5-phenyl group of the secondary ligand and the rigid macrocyclic framework.

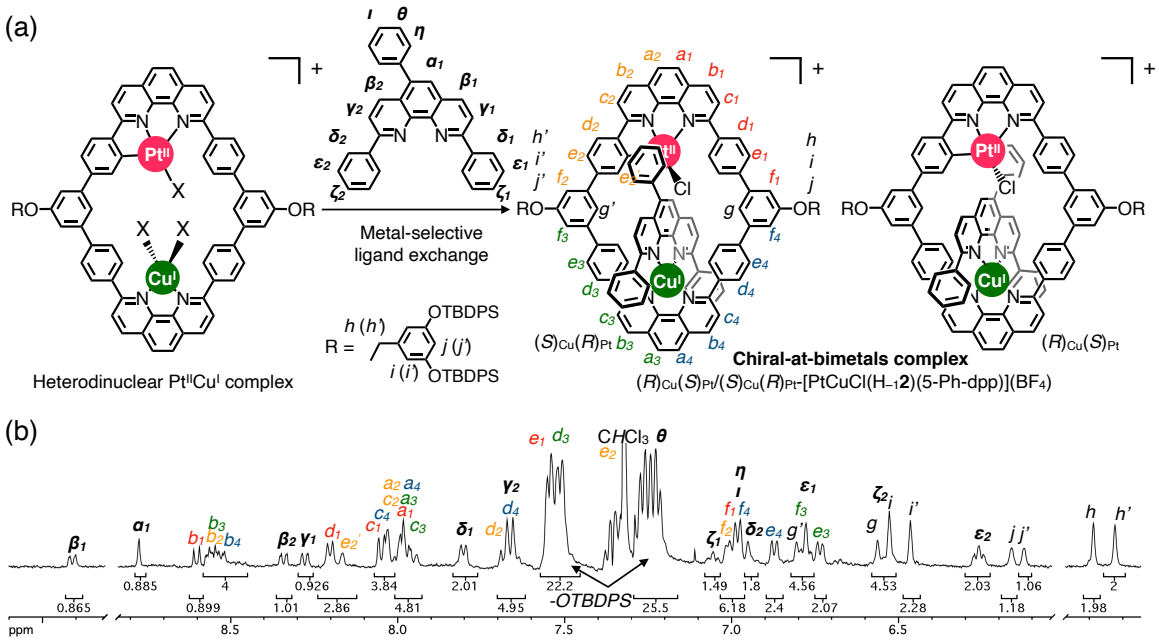

Figure 5. The diastereoselective synthesis of chiral-at-bimetals heterodinuclear $Pt^{II}Cu^{I}$ complexes: (a) Synthetic scheme of the chiral-at-bimetals heterodinuclear $(R)_{Cu}(S)_{Pt}$-/$(S)_{Cu}(R)_{Pt}$-[PtCuCl(H_{-1}**2**)(5-Ph-dpp)](BF_4) complexes; (b) ^{1}H NMR spectrum (500 MHz, 300 K, $CDCl_3/CD_3CN$ = 9:1) for the racemic mixture of $(R)_{Cu}(S)_{Pt}$-/$(S)_{Cu}(R)_{Pt}$-[PtCuCl(H_{-1}**2**)(5-Ph-dpp)](BF_4).

5. Conclusions and perspectives

In this study, anisotropic and asymmetric arrangement of metal ions with symmetric bisphenanthroline macrocycle was achieved in three ways: protonation-induced formation of metal-assembled nanofibers, sequential introduction of two different metal ions to synthesize macrocyclic heterodinuclear complexes, and the diastereoselective synthesis of chiral-at-bimetals a heterodinuclear $Pt^{II}Cu^{I}$ complex. These findings would provide clues for developing unique anisotropic or asymmetric materials with macrocyclic building blocks such as electronical nanofibers, highly anisotropic metal clusters synthesis, and unprecedented asymmetric catalysts based on the heterometallic arrangement.

References

[1] M. Shionoya *et al*., *J. Am. Chem. Soc.* **2014**, *136*, 17946–17949. [2] M. Shionoya *et al*., *Chem. Asian J.* **2013**, *8*, 1368–1371. [3] M. Shionoya *et al*., *Inorg. Chem.* **2012**, *51*, 1508–1515.

Abbreviations

ATR	attenuated total reflection
Abs	absorbance
AcOEt	ethyl acetate
AFM	atomic force microscope
bpy	2,2'-bipyridine
calcd.	calculated
CCDC	Cambridge Crystallographic Data Center
COSY	correlation spectroscopy
d	doublet
dd	double doublet
δ	chemical shift
DLS	dynamic light scattering
DMF	dimethyl formamide
DMSO	dimethyl sulfoxide
dpp	2,9-diphenyl-1,10-phenanthroline
EDA	ethylenediamine
EDS	energy dispersive X-ray spectroscopy
en	ethylenediamine
eq	equivalent
ESI	electrospray ionization
EtOH	ethanol
Et_2O	diethyl ether
GOF	goodness of fit
h	hours
J	coupling constant
l	cell length
L	ligand
λ	wavelength
m	multiplet
m	mass
M	metal ions / molar [mol/L]
Me	methyl
Min	minutes
MM	molecular mechanics
MS	mass spectrometry
n-	normal
NMR	nuclear magnetic resonance
ORTEP	Oak Ridge thermal-ellipsoid plot
OTf	trifluoromethanesulphonate
PdI	polydispersity index

Ph	phenyl
phen	1,10-phenanthroline
PhMe	toluene
ppm	parts per million
PXRD	powder X-ray diffraction
θ	angle
ROESY	rotating frame Overhauser effect spectroscopy
rt	room temperature
STEM	scanning transmission electron microscope
t	triplet
TBA	*n*-tetrabutylammonium
TBDPS	*t*-butyl(diphenyl)silyl
TMS	trimethylsilane
TOF	time of flight
TRISPHAT	tris(tetrachloro-1,2-benzenediolato) phosphate(V)
UV-Vis	ultraviolet-visible
XRD	X-ray diffraction
z	charge number
Z	hydrodynamic radius

Contents

Chapter 1.

General Introduction

1–1. Metal ions in biological systems

Metal ions are the essential components of biological systems. They play various roles in living activities such as storage, transfer, and activation of small molecules.[1] For instance, hemoglobin and myoglobin are well-known proteins for storage and transfer of molecular oxygen in blood and muscle, respectively, which possess four heme subunits composed of a porphyrin ring with a Fe^{II} center for each in common (Figure 1-1a).[2] The Fe^{II} centers are indispensable for the function due to their reversible binding ability to molecular oxygen. A porphyrin ring is also included in chlorophylls with a Mg^{II} ion at its center instead which can efficiently absorb light and convert light energy into electrochemical energy through photosynthesis (Figure 1-1b).[3] Other marvelous functions of metal ions can be seen in metalloenzymes in which two or more metal ions are confined in a nanospace to induce their cooperative catalytic activities. For example, cytochrome *c* oxidase in mitochondria has multiple heme units, a dinuclear Cu unit and a mononuclear Cu unit located with certain distances between them to allow efficient electron transfer between the metal centers to enable excellent redox catalytic reactions (Figure 1-1c).[4] Such diverse and efficient functions of metalloproteins are derived from the various ionic radius, charge number, Lewis acidity, redox potential, and other properties of metal ions, as well as the synergetic effects arising from different combination, numbers, and relative positions of metal centers.

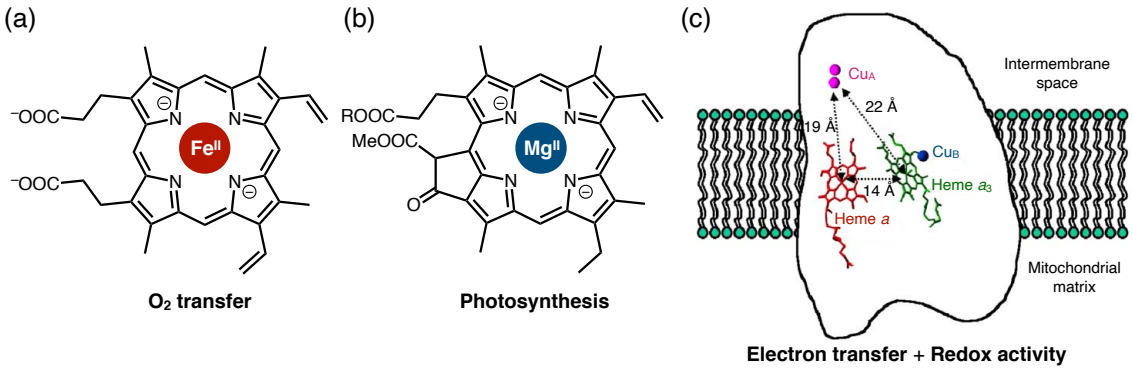

Figure 1–1. Functional metal centers in biological systems: (a) heme in hemoglobin; (b) chlorophyll *a*; (c) cytochrome *c* oxidase. Figure 1-1(c) is reproduced from *J. Inorg. Biochem.* **2005**, *99*, 324–336,[4] Copyright 2005 Elsevier.

1–2. Artificial multinuclear metal complexes

Aiming at the development of functional materials comparable to the metalloproteins, a variety of multinuclear metal complexes have been synthesized to demonstrate their array-specific interactions and properties. For example, Osuka and co-workers developed a dimeric porphyrin ligand connected by a *o*-phenylene linker to synthesize a dinuclear Zn^{II} complex (Figure 1-2a).[5] They revealed that the two Zn^{II} porphyrin units electronically interacted with each other to show highly decreased oxidation potential compared to the corresponding mononuclear Zn^{II} complex. Furthermore, the same group also succeeded in the synthesis of a linearly-arrayed multinuclear Zn^{II} complex to demonstrate its high electrical conductivity along the Zn^{II} array (Figure 1-2b).[6] On the other hand, cyclic porphyrin arrays have been studied to develop light harvesting complexes as exemplified by the macrocyclic hexanuclear Zn^{II} complex whose great light absorbing ability could be attributed to the efficient energy migration between each porphyrin unit (Figure 1-2c).[7] Apart from the intramolecular electronic interactions, such cyclic porphyrin arrays could also be applied to catalytic reaction by precisely fixing and activating multiple substrates by coordination bonding formation at Zn^{II} centers as reported by Sanders' group (Figure 1-2d).[8] These examples strongly suggested that the arrangement mode of metal ions is very important to control the properties and functions of multinuclear metal complexes such as redox potential, optical properties, magnetic properties, electrical conductivity, catalytic activities, and so on.[9]

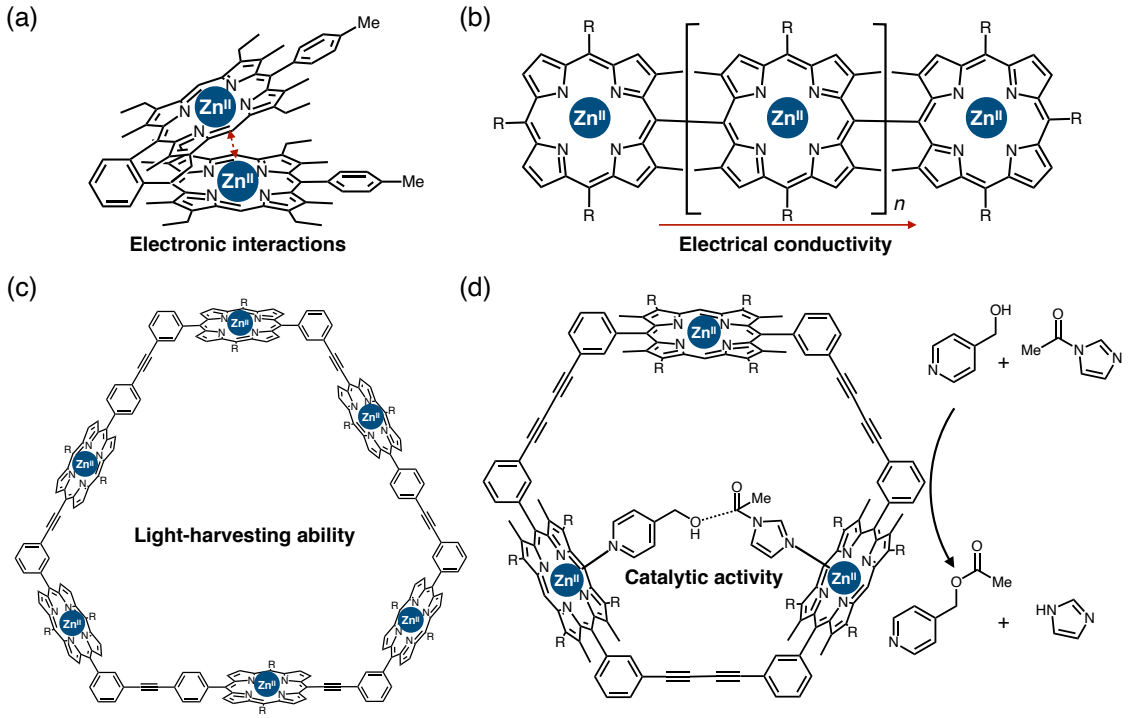

Figure 1–2. Representative examples of porphyrin-based multinuclear Zn^{II} complexes: (a) a dinuclear complex[5]; (b) a linearly-connected multinuclear complex[6a]; (c) a macrocyclic hexanuclear complex[7a]; (d) a macrocyclic trinuclear complex with catalytic activity.[8a]

1–3. Macrocycles for metal arrangement

As exemplified by the porphyrin ring above, macrocycle is an attractive scaffold for metal arrangement because it can strongly bind to metal ions with multiple interactions and chelate effect (Figure 1-3a).[10] For example, the macrocyclic amine ligand with four inward nitrogen atoms, named cyclam, can provide four coordination bonds (Figure 1-3b),[11] while a series of cyclic ether ligands, named crown ether, have multiple inward oxygen atoms to form size-dependent cation-dipole interactions with metal ions (Figure 1-3c).[12] The thermodynamically- and kinetically-stable macrocyclic metal complexes can be incorporated into the design of multinuclear metal complexes without losing the coordination ability. Besides the covalently-connected macrocyclic ligands as shown in the last section, self-assembly of the metallomacrocycles is an alternative way to access metal arrangement as exemplified by the infinite one-dimensional arrangement of K^+ ions along the self-assembling macrocycles (Figure 1-3d).[13]

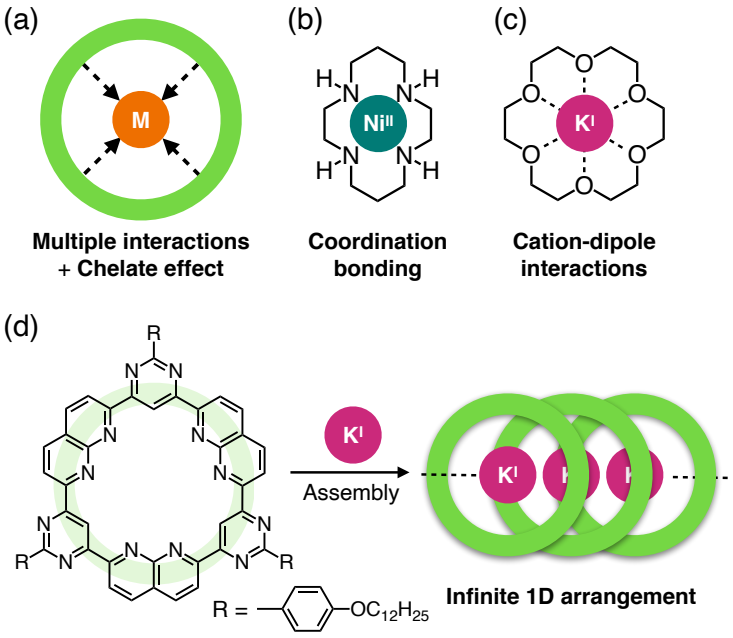

Figure 1–3. Representative examples of macrocyclic metal complexes: (a) schematic representation of a macrocyclic metal complex; (b) a Ni^{II}-cyclam complex[11]; (c) a K^+-18-cronwn-6 complex[12]; (d) infinite 1D arrangement of K^+ ions based on self-assembly of macrocycles.[13]

As for macrocyclic multinuclear metal complexes, macrocyclic scaffolds have another advantage that arrangement of metal ions in the macrocycle can be defined well due to the rigidity of the macrocyclic framework. In addition, they can provide metal-surrounded nanospace which is useful for molecular recognition[14] and reaction field (Figure 1-4a).[15] For example, Taglietti and co-workers reported a use of bimetallic cryptates for size-selective anion recognition by utilizing the inward two metal centers and the rigid macrocyclic framework (Figure 1-4b).[15a] The effectiveness of metal-surrounded reaction field was demonstrated by the macrocyclic dinuclear Cu^{II} complex of Maverick's group, in which two carbon dioxide molecules were entrapped in close proximity and their reductive dimerization into oxalic acid efficiently took place through electron transfer from the copper centers which is derived from the coexisting ascorbate. To realize these functions, a well-designed inner structure of macrocyclic scaffold is necessary.

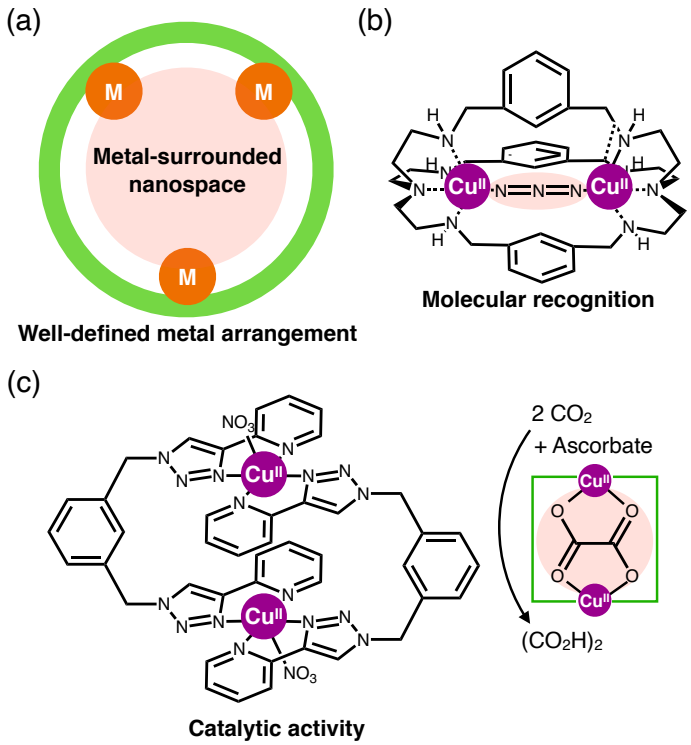

Figure 1–4. Representative examples of macrocyclic multinuclear metal complexes: (a) schematic representation of a macrocyclic multinuclear complex; (b) molecular recognition with a macrocyclic dinuclear Cu^{II} complex[14a]; (c) catalytic reaction with a macrocyclic dinuclear Cu^{II} complex.[15a]

1–4. Bisphenanthroline macrocyclic metal complexes

As a macrocyclic scaffold for metal arrangement, our group has previously developed bisphenathroline macrocycles with two inward phenanthroline coordination sites and a rigid aromatic framework (Figure 1-5a). By utilizing the macrocyclic scaffold, homometallic and heterometallic arrangement were achieved with particular pairs of Ag^{I}, Cu^{I}, and Zn^{II} ions (Figure 1-5b).[16] A dinuclear Pd^{II} complex was also synthesized to show its one-dimensional self-assembly into nanofibers containing anisotropic Pd^{II} arrangement (Figure 1-5c).[17] These studies ensured that the bisphenthroline macrocycle is a desirable scaffold for arrangement of two metal ions in the cavity as well as for one-dimensional arrangement of the introduced metal ions by self-assembly. However, the applicable metal ions were limited especially in the case of the heterometallic arrangement and the one-dimensional arrangement, and therefore the application of the arranged metal centers was limited. Thus, arrangement method applicable to various metal ions were required to fully utilize the attractive scaffold for unique function materials as demonstrated by molecular recognition with a dinuclear Ag^{I} complex of the similar ligand (Figure 1-5d).[18]

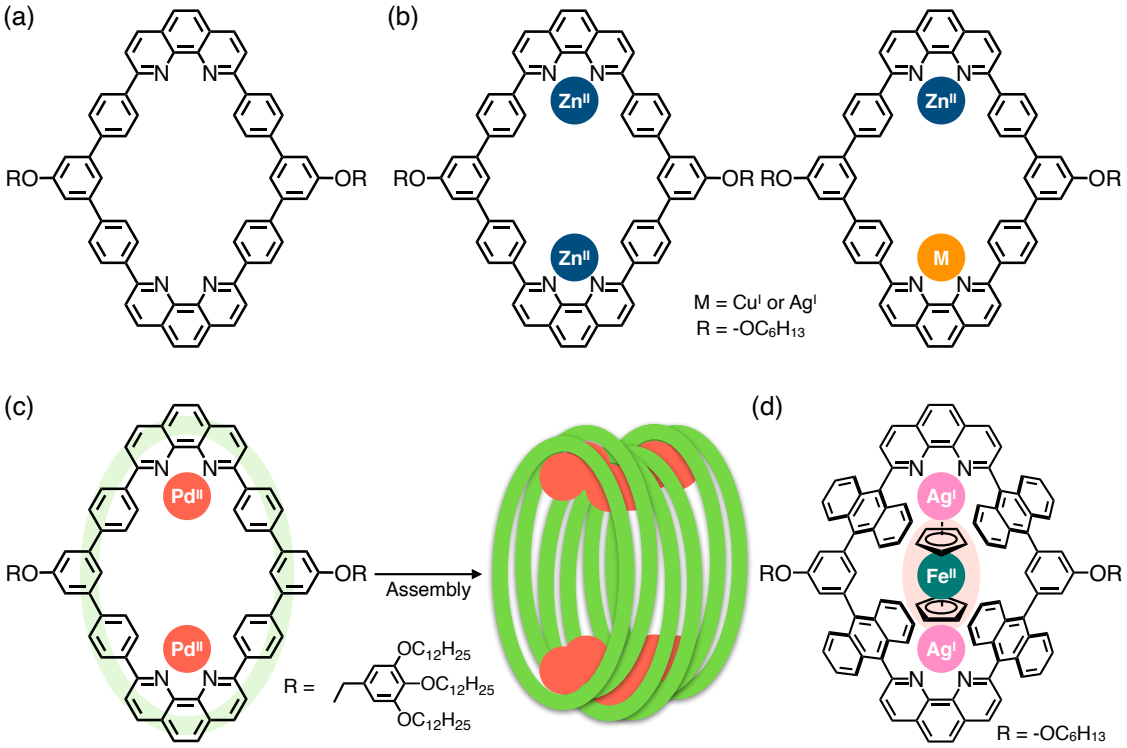

Figure 1–5. Examples of bisphenanthroline macrocyclic metal complexes: (a) a chemical structure of bisphenanthroline macrocyclic framework; (b) Zn^{II}-containing homodinuclear and heterodinulear complexes[16]; (c) 1D assembly of homodinuclear Pd^{II} complexes[17]; (d) inclusion of ferrocene in a homodinuclear Ag^{I} complex.[18]

1–5. The aim of this research

In this work, I aimed at developing novel methodologies for various metal arrangement by fully utilizing the bisphenanthroline macrocyclic scaffold (Figure 1-6): (i) infinite one-dimensional metal arrangement by utilizing electrostatic interactions, (ii) kinetically-controlled complexation with two different metal ions, and (iii) arrangement of two different metal ions with chirality at both metal centers.

Chapter 2 describes the infinite one-dimensional metal arrangement. This method utilizes the protonation of phenanthroline moieties and electrostatic interactions between the resulting cationic macrocycles and anionic metal complexes. A variety of anionic metal complexes with different size, charge number and coordination geometry could be arranged in the same manner to afford various metal-assembled nanofibers.

Chapter 3 represents kinetically-controlled heterometallic arrangement. In this method, the firstly introduced metal ion formed a kinetically-stable mononuclear complex with the bisphenanthroline macrocycle, to which a secondary metal ion could be incorporated to realize several heterometallic arrangements. The difference in inertness and coordination geometries of the introduced metal ions also enabled metal-selective ligand exchange to afford stable heterodinuclear metal complexes.

Chapter 4 describes the synthesis of unprecedented chiral-at-bimetals heterodinuclear complexes. Desymmetrized structure of the heterodinuclear metal complexes was utilized to introduce metal-centered chirality at one metal center by metal-selective ligand exchange reaction with a secondary achiral ligand. The precise design of the secondly incorporated ligand resulted in a transfer of structural information from one metal center to another to allow spontaneous formation of one diastereomeric pair of chiral-at-bimetals complex.

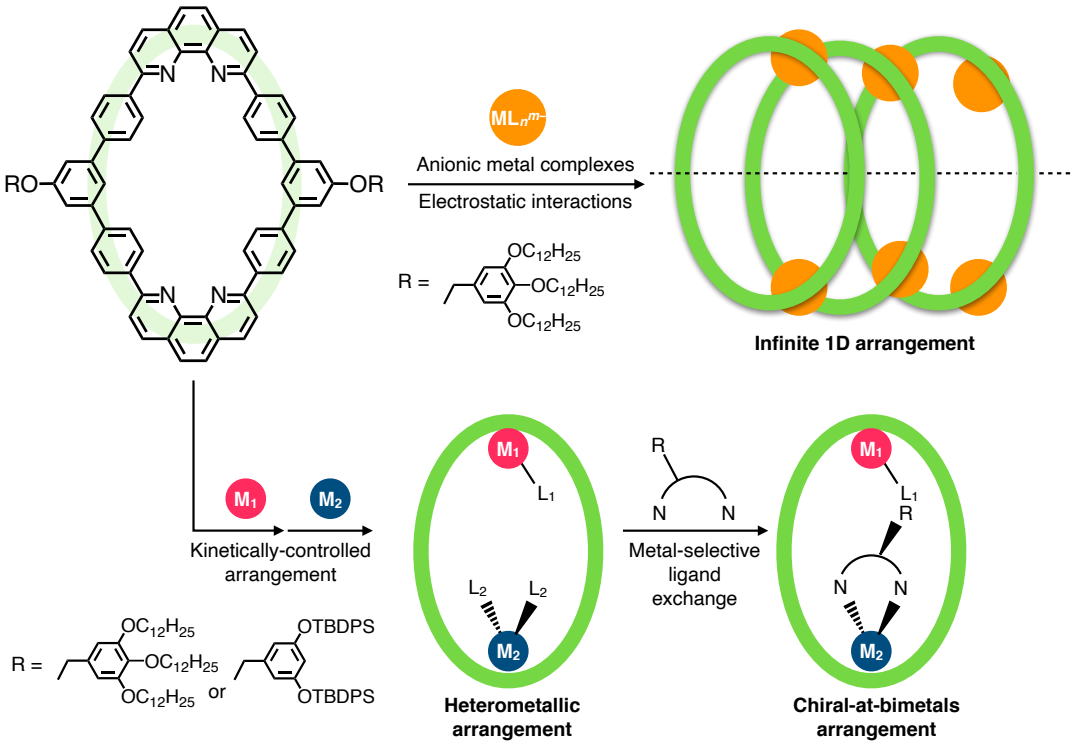

Figure 1–6. Outline of this research: infinite one-dimensional arrangement of anionic metal complexes, kinetically-controlled synthesis of heterodinuclear metal complexes, and construction of chiral-at-bimetals heterodinuclear complexes.

1-6. References

[1] Crichton, R. R. 著; 塩谷光彦 訳, 「クライトン生物無機化学　第 2 版」 東京化学同人, 2016.

[2] (a) Perutz, M. F.; Rossmann, M. G.; Cullis, A. F.; Muirhead, H.; Will, G.; North, A. C. T. *Nature* **1960**, *185*, 416–422. (b) Kendrew, J. C.; Dickenrson, R. E.; Standberg, B. E.; Hart, R. G.; Davies, D. R. *Nature* **1960**, *185*, 422–427.

[3] (a) Umena, Y.; Kawakami, K.; Shen, J.-R.; Kamiya, N. *Nature* **2011**, *473*, 55–61. (b) Qin, X.; Suga, M.; Kuang, T.; Shen, J.–R. *Science* **2015**, *348*, 989–995.

[4] Brunori, M.; Giuffre, A; Aarti, P. *J. Inorg. Biochem.* **2005**, *99*, 324–336.

[5] Osuka, A.; Nakajima, S.; Maruyama, K.; Mataga, N.; Asahi, T.; Yamazaki, I.; Nishimura, Y.; Ohno, T.; Nozaki, K. *J. Am. Chem. Soc*. **1993**, *115*, 4577–4589.

[6] (a) Yoon, D. H.; Lee, S. B.; Yoo, K.–H.; Kim, J.; Lim, J. K.; Aratani, N.; Tsuda, A.; Osuka, A.; Kim, D. *J. Am. Chem. Soc*. **2003**, *125*, 11062–11064. (b) Wytko, J. A.; Ruppert, R.; Jeandon, C.; Weiss, J. *Chem. Commun*. **2018**, *54*, 1550–1558.

[7] (a) Nakamura, Y.; Aratani, N.; Osuka, A. *Chem. Soc. Rev*. **2007**, *36*, 831–845. (b) Li, J.; Ambroise, A.; Yang, S. I.; Diers, J. R.; Seth, J.; Wack, C. R.; Bocian, D. F.; Holten, D.; Lindse, J. S. *J. Am. Chem. Soc*. **1999**, *121*, 8927–8940.

[8] (a) Mackay, L. G.; Wylie, R. S.; Sanders, J. K. M. *J. Am. Chem. Soc*. **1994**, *116*, 3141–3142. (b) Clyde-Watson, Z.; Vidal-Ferran, A.; Twyman, L. J.; Walter, C. J.; McCallien, D. W. J.; Fanni, S.; Bampos, N.; Wylie, R. S.; Sanders, J. K. M. *New J. Chem*. **1998**, 493–502.

[9] (a) Raynal, M.; Ballester, P.; Vidal-Ferran, A.; Leeuwen, P. W. N. M. *Chem. Soc. Rev*. **2014**, *43*, 1734–1787. (b) Raynal, M.; Ballester, P.; Vidal-Ferran, A.; Leeuwen, P. W. N. M. *Chem. Soc. Rev*. **2014**, *43*, 1660–1733. (c) Kondo, M.; Masaoka, S. *Acc. Chem. Res*. **2020**, *53*, 2140–2151.

[10] Lindoy, L. F.; Park, K.-M.; Lee, S. S. *Chem. Soc. Rev*. **2013**, *42*, 1713–1727.

[11] Barefield, E. K.; Mocella, M. T. *J. Am. Chem. Soc*. **1975**, *97*, 4238–4246.

[12] Bradshaw, J. S.; Izatt, R. M. *Acc. Chem. Res*. **1997**, *30*, 338–345.

[13] Petitjean, A.; Cuccia, L. A.; Schmutz, M.; Lehn, J.-M. *J. Org. Chem*. **2008**, *73*, 2481–2495.

[14] (a) Amendola, V.; Fabbrizzi, L.; Mangano, C.; Pallavicini, P.; Poggi, A.; Taglietti, A. *Coord. Chem. Rev*. **2001**, *219–221*, 821-837. (b) Nakamura, T.; Kaneko, Y.; Nishibori, E.; Nabeshima, T. *Nat. Commun*. **2017**, *8*, 129. (c) Yanagisawa, M.; Tashiro, K.; Yamasaki, M.; Aida, T. *J. Am. Chem. Soc*. **2007**, *129*, 11912–11913. (d) Anderson, S.; Anderson, H. L.; Bashall, A.; McPartlin, M.; Sanders, J. K. M. *Angew. Chem. Int. Ed. Engl*. **1995**, *34*, 1096–1099.

[15] (a) Pokharel, U. R.; Fronczek, F. R.; Maverick, A. W. *Nat. Commun*. **2014**, *5*, 5883. (b) Nath, B. D. N.; Takaishi, K.; Ema, T. *Catal. Sci. Technol*, **2020**, *10*, 12–34. (c) Schulze, M.; Kunz, V.;

Frischmann, P. D.; Würthner, F. *Nat. Chem*. **2016**, *8*, 576–583.

[16] Kuritani, M.; Tashiro, S.; Shionoya, M. *Inorg. Chem*. **2012**, *51*, 1508–1515.

[17] Kuritani, M.; Tashiro, S.; Shionoya, M. *Chem. Asian J*. **2013**, *8*, 1368–1371.

[18] Omoto, K.; Tashiro, S.; Kuritani, M.; Shionoya, M. *J. Am. Chem. Soc.* **2014**, *136*, 17946–17949.

Chapter 2.

Protonation-induced self-assembly of bisphenanthroline macrocycles into metal-assembled nanofibers

2–1. Introduction

As described in Chapter 1, arrangement mode of metal ions is an essential factor for controlling the property and function of multinuclear metal complexes. From this point of view, control of dimensionality is important especially to develop anisotropic functional materials.[1] As for one-dimensional materials, various metal arrangement-specific functions and properties have been explored such as electronic conductivity,[2] oxidation state,[3] magnetism,[4] optical properties,[5] and so on. As a representative example, Nishihara and co-workers have reported the length-selective synthesis of molecular nanowires with excellent electronic conductivity based on one-dimensional coordination bond formation.[6a] They also demonstrated that the redox potential and electronic conductivity could be controlled by the number and arrangement modes of metal ions (Figure 2-1a).[6b]

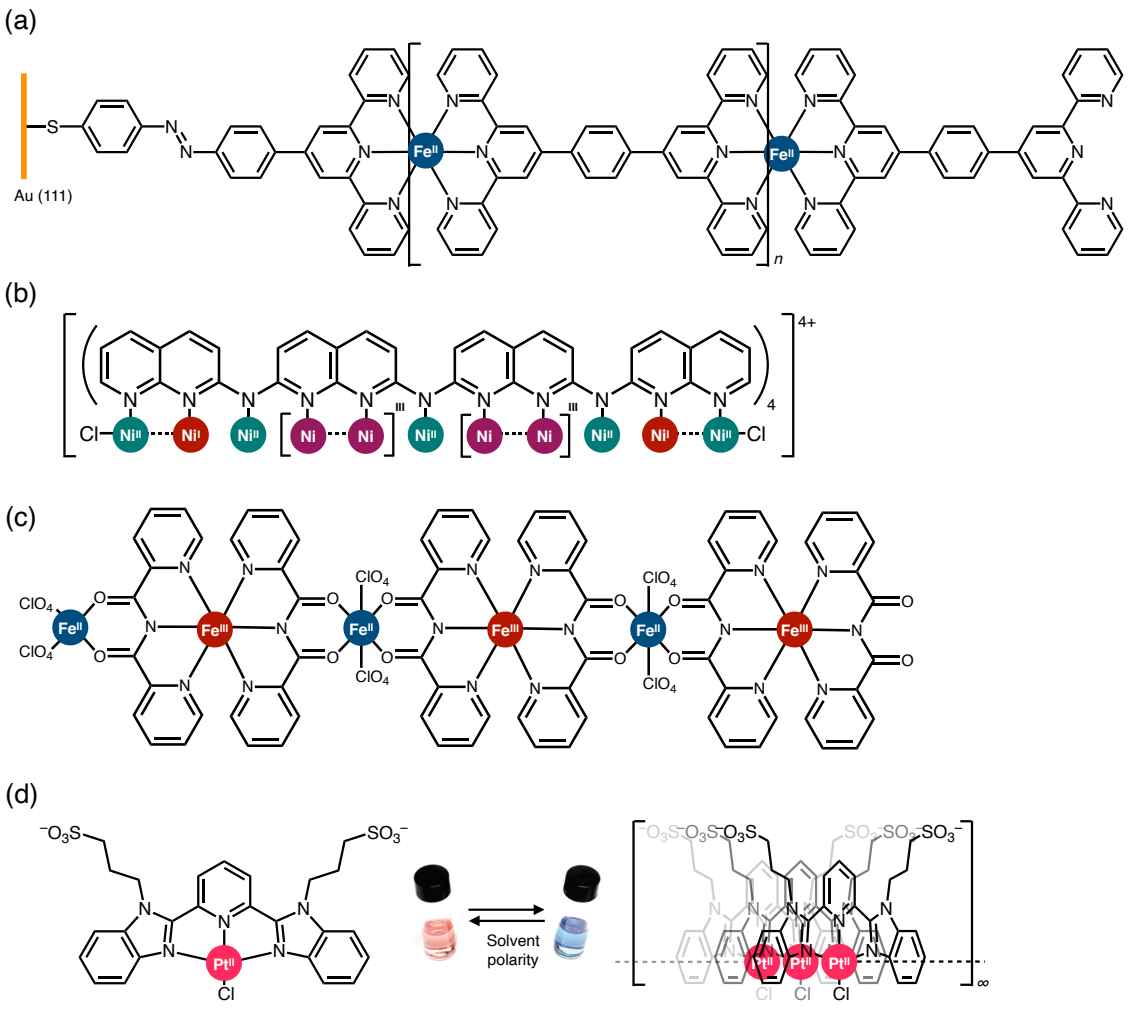

Figure 2–1. Special properties of one-dimensionally-arranged metal ions: (a) arrangement-specific electronic conductivity;[6b] (b) array-specific oxidation state;[7] (c) array-specific spin state;[8] (d) array-specific optical property.[9] Figure 2-1(d) is reproduced from *J. Am. Chem. Soc.* **2011**, *133*, 12136-12143,[9] Copyright 2011 American Chemical Society.

For one-dimensional arrangement of metal ions, various kinds of bonding and interactions have been utilized as driving force. Among them, metal-specific bonding and interactions have been extensively studied on complexes with one-dimensional multidentate ligands,[10] coordination polymers,[11] and linear arrangement of metal complexes by metal-metal interactions.[12] Although coordination bonding and metal-metal interactions are powerful tools to definitely program the positions of metal ions, the assembly modes are highly dependent on the choice of metal ions. On the other hand, electrostatic interactions such as cation-dipole interactions[13] and ion pair formation[14] can be an alternative driving force which enables arrangement of various metal ions with a common scaffold. However, the target ion is generally limited to alkaline metals[13a–d,14b,14d] or alkaline earth metals[14b] and otherwise coordination bonding formation is necessary[14a,14c] which descopes the potential applications. To overcome this problem, development of a novel methodology for one-dimensional metal arrangement applicable to a wide scope of metal ions was required.

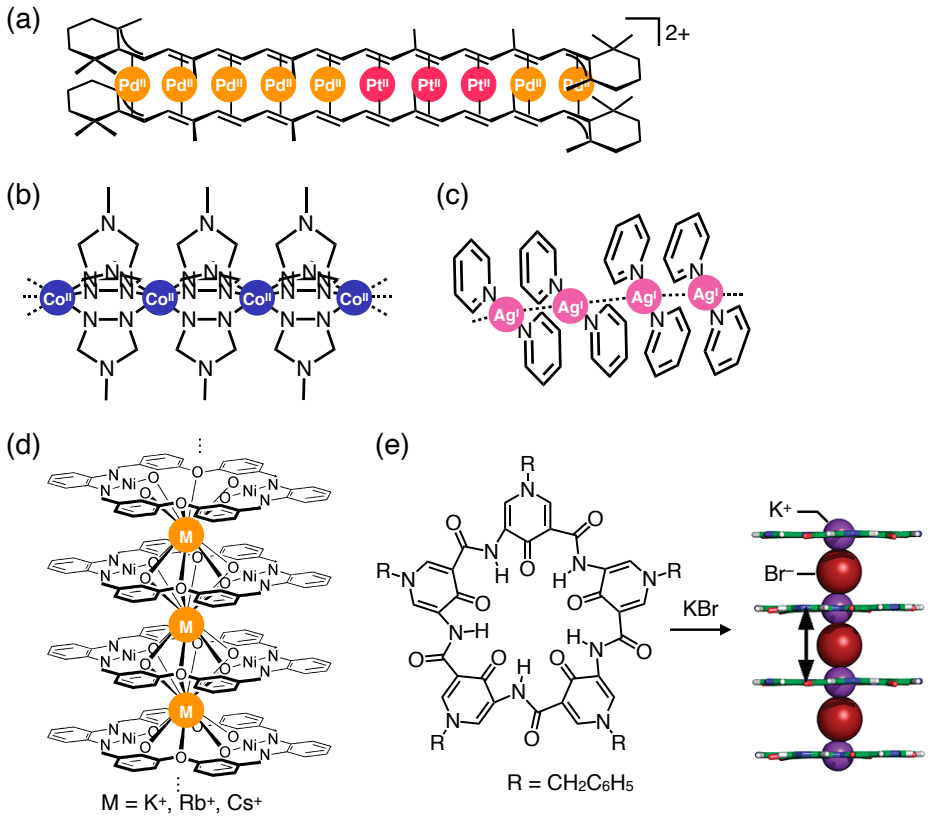

Figure 2–2. One-dimensional arrangement of metal ions with different driving forces: (a) linear multinuclear complexation;[15] (b) coordination bond network;[16] (c) metal-metal interactions;[17] (d) cation-dipole interactions;[18] (e) ion pairs.[19] Figure 2-2(d) is reproduced from *Inorg. Chem.* **2016**, *55*, 810-821,[18] Copyright 2016 American Chemical Society, and Figure 2-2(e) is reproduced from *J. Am. Chem. Soc.* **2011**, *133*, 13930-13933,[19] Copyright 2011 American Chemical Society.

This chapter describes a novel methodology for one-dimensional assembly of a variety of metal ions with bisphenanthroline macrocycle **1** and electrostatic interactions as a driving force. In order to induce electrostatic interactions, protic acid of anionic metal complexes was mixed with **1** to afford an ionic pair of anionic metal complexes and cationic **1** with protons at two phenanthroline moieties. The two ionic molecules form alternating stacking on each other to form supramolecular nanofibers arrayed with metal ions (Figure 2-3). Since this process does not include coordination bond formation, various metal-containing protic acids with different size, charge number, and coordination geometry such as $HAuCl_4$, H_2PtCl_6, and $H_3PMo_{12}O_{40}$ could be used to construct a variety of metal-assembled nanofiber. Furthermore, the assembled metal ions could be chemically reduced to afford unique reduced states of assembled metal ions: Au nanoparticles dispersible in organic solvents and Mo^{VI}/Mo^{V}-mixed balance nanofibers.

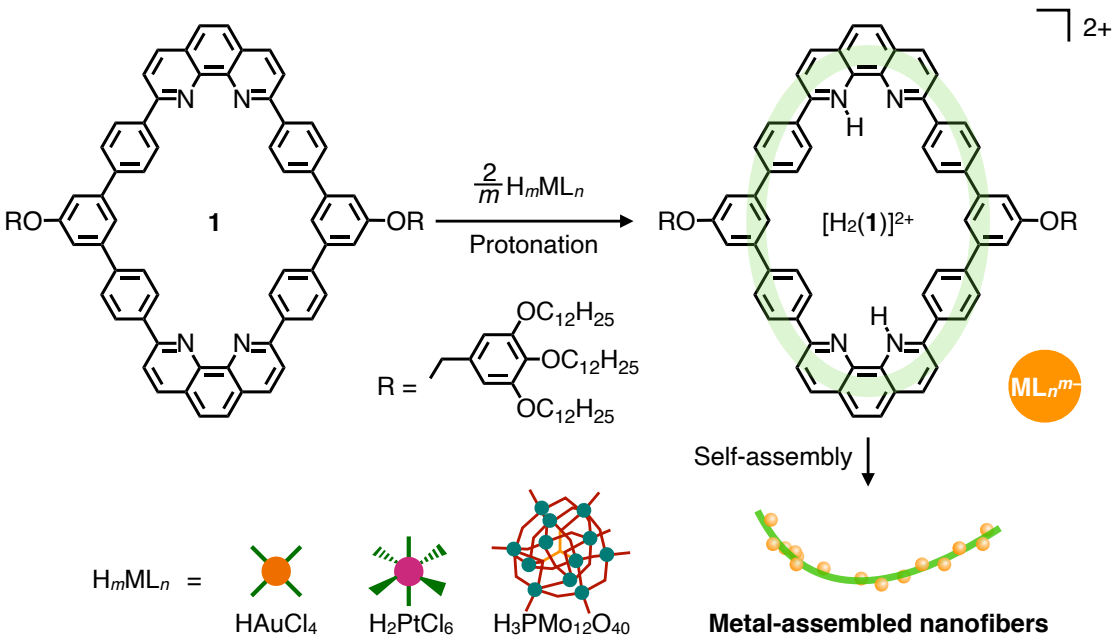

Figure 2–3. Schematic representation of protonation-induced assembly of **1** into metal-assembled nanofibers.

2–2. Construction of metal-assembled nanofibers

The bisphenanthroline macrocycle **1** was previously designed as a ligand for a dinuclear Pd^{II} complex.[20] It has been reported that both **1** and the Pd^{II} dinuclear complex can form supramolecular nanofibers in cyclohexane and $CHCl_3/CH_3CN$ (10:1), respectively, due to the existence of lipophilic long alkyl side chains for inducement of solvophobic effect and enhancement of solubility. In this study, the two phenanthroline moieties serve as basic sites which are protonated after mixing with protic acids. The rigid macrocyclic framework is important in regulating the direction of assembly (Figure 2-4).

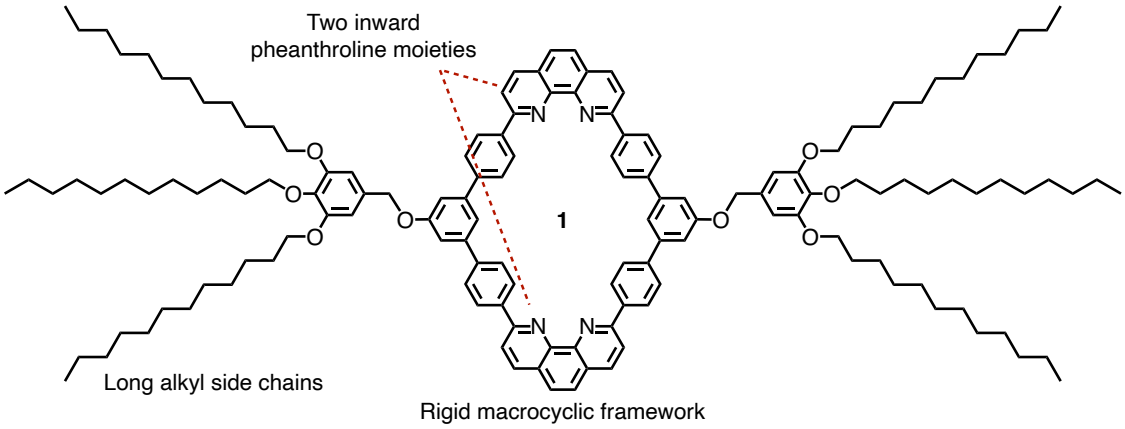

Figure 2–4. Molecular structure of macrocycle **1**.

2–2–1. Au^{III}-assembled nanofibers

Protonation of 1 by addition of $HAuCl_4 \cdot 4H_2O$

A protic acid $HAuCl_4$ was firstly chosen as a Au^{III} source because Au complexes are known to possess attractive physical and chemical properties including the photophysical properties[21] and redox activities.[22] Protonation of the phenanthroline sites of **1** was investigated by ^1H NMR spectroscopic titration experiment with $HAuCl_4 \cdot 4H_2O$ in $CDCl_3/CD_3CN$ (10:1) (Figure 2-5). As a result, the initially sharp signals showed significant broadening upon addition of $HAuCl_4$. After adding 2.0 eq of $HAuCl_4 \cdot 4H_2O$, the aromatic signals almost completely disappeared while some signals could be observed in the aliphatic region assignable to the alkyl side chains, indicating changes in the chemical environment at the macrocyclic moiety. ESI-TOF MS spectrum of the resultant 1:2 mixture of **1** and $HAuCl_4$ clearly showed protonated **1** as well as diprotonated **1** with $AuCl_4^-$ as a counter anion (*m*/*z* for $[H(\mathbf{1})]^+$: 2131.48; found: 2132.62; *m*/*z* for $[[H_2(\mathbf{1})][AuCl_4]]^+$: 2471.34; found: 2471.48, respectively, Figure 2-6). From these results, it is likely that protonation of phenanthroline moieties with $HAuCl_4$ took place, which is reasonable judging from the strong acidity of $HAuCl_4$.

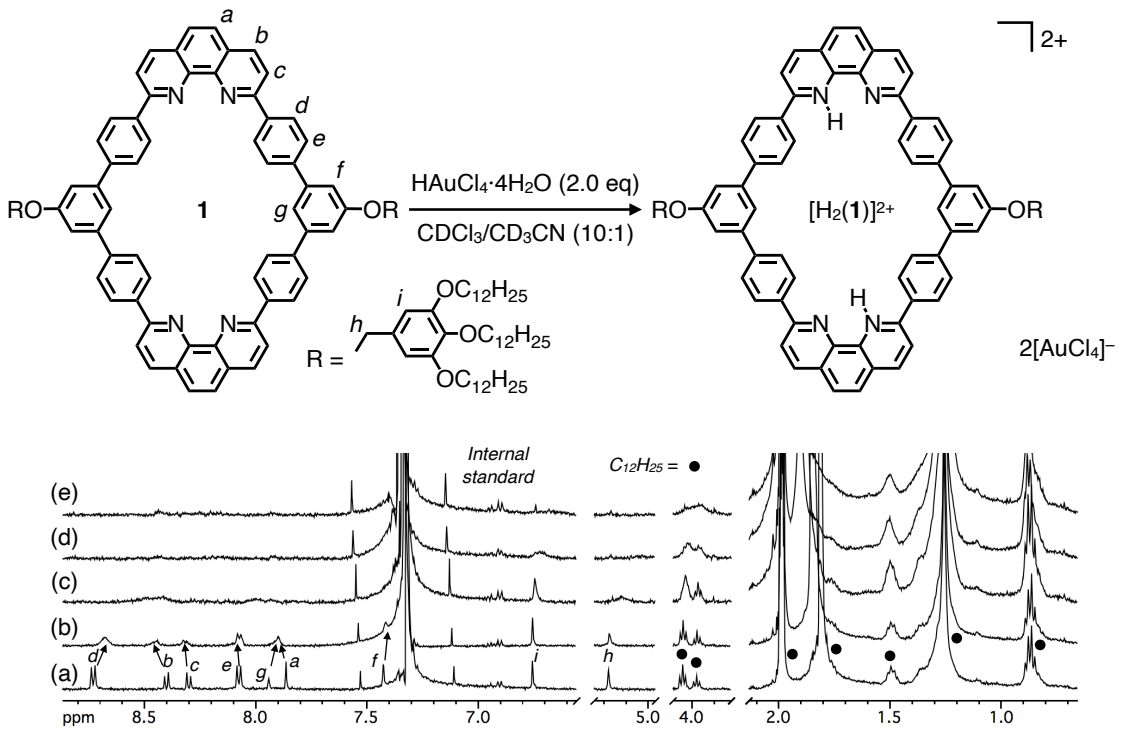

Figure 2–5. Partial ^1H NMR spectra (500 MHz, $CDCl_3/CD_3CN$ = 10/1, 300 K) of a mixture of **1** and different amounts of $HAuCl_4 \cdot 4H_2O$: (a) [**1**] = 84 μM, $HAuCl_4 \cdot 4H_2O$ = 0 eq; (b) $HAuCl_4 \cdot 4H_2O$ = 0.5 eq; (c) $HAuCl_4 \cdot 4H_2O$ = 1.0 eq; (d) $HAuCl_4 \cdot 4H_2O$ = 1.5 eq; (e) $HAuCl_4 \cdot 4H_2O$ = 2.0 eq. Anisole is included in the reaction mixture as an internal standard.

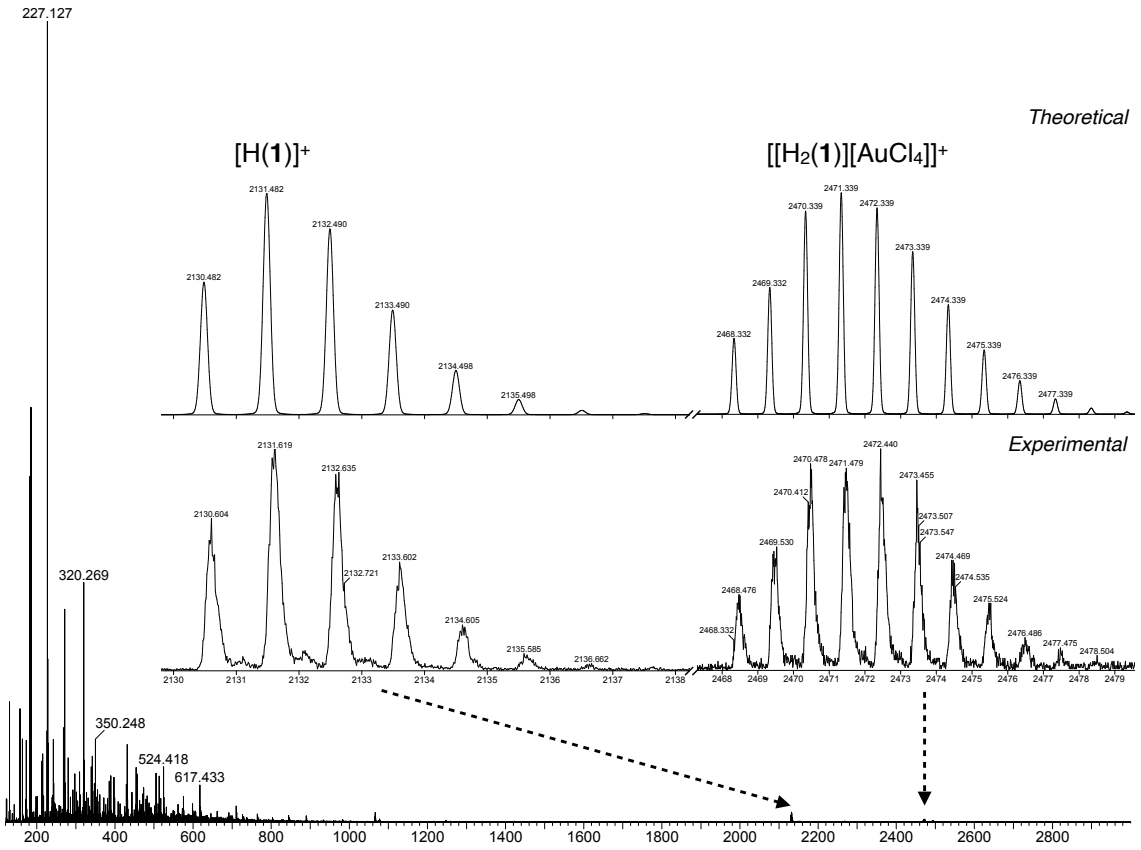

Figure 2–6. ESI-TOF MS spectrum (positive) of the 1:2 mixture of **1** and $HAuCl_4$

Protonation of **1** with $HAuCl_4$ was further investigated by UV-vis titration experiment (Figure 2-7). As the amount of $HAuCl_4$ increased, the absorption maximum around 310 nm showed significant decrease, meanwhile wide absorption shoulder appeared in the range from 360 nm to 550 nm. Since these spectral changes can be attributed to protonation of **1**, an apparent protonation constant could be calculated by the least-square fitting of the changes in absorbance (Figure 2-8). Consequently, the equilibrium constant K_1 (= [[H(**1**)][$AuCl_4$]]/[**1**][$HAuCl_4$]) and K_2 (=[[H_2(**1**)][$AuCl_4$]$_2$]/[[H(**1**)][$AuCl_4$]][$HAuCl_4$]) for the first and second protonation at 20 °C were estimated to be $(5.7 \pm 0.2) \times 10^5$ M^{-1} and $(2 \pm 1) \times 10^5$ M^{-1}, respectively. These values are almost comparable to the reported value for the reaction between 2,9-diaryl-1,10-phenanthroline and a strong acid.[23] From these values, it was concluded that two phenanthroline moieties of **1** are almost completely protonated by addition of 2.0 eq of $HAuCl_4 \cdot 4H_2O$.

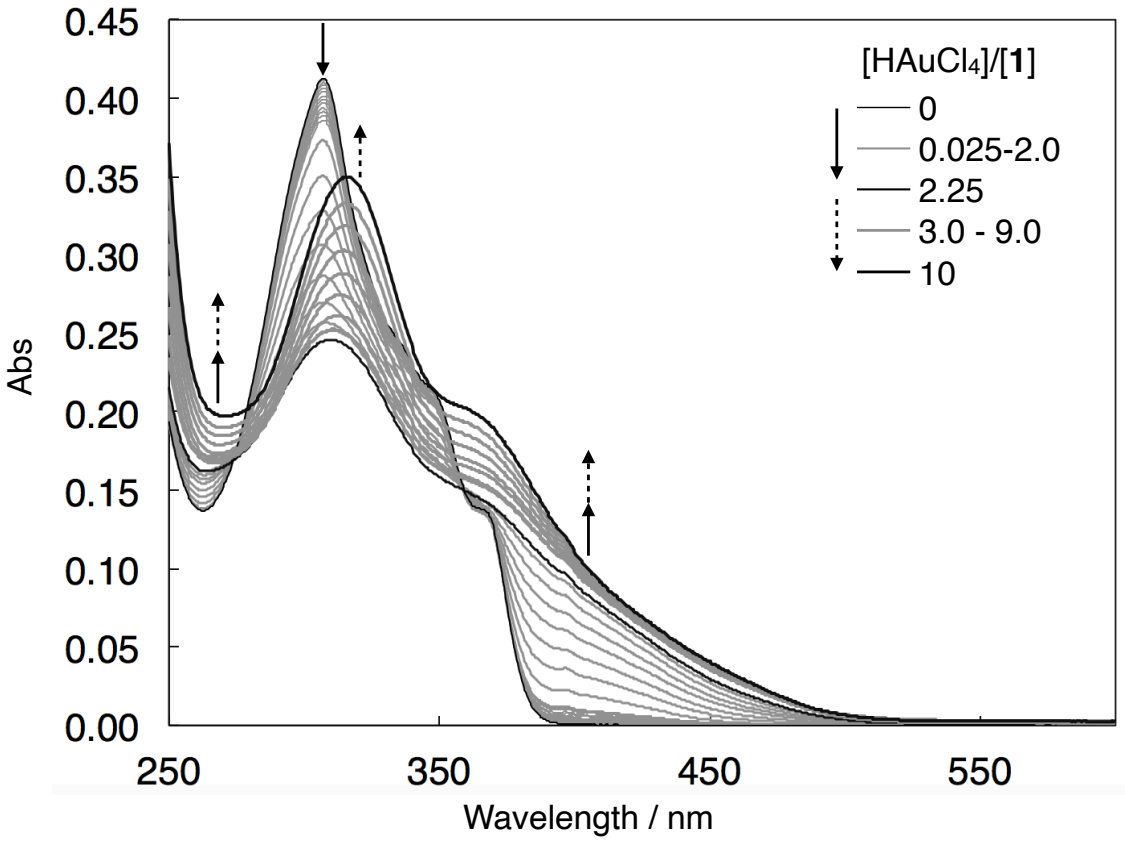

Figure 2–7. UV-vis spectra ($CHCl_3/CH_3CN$ = 10/1, 20 °C, [**1**] = 29 μM, l = 0.1 cm)) of a mixture of **1** and different amounts of $HAuCl_4 \cdot 4H_2O$ up to 10 eq.

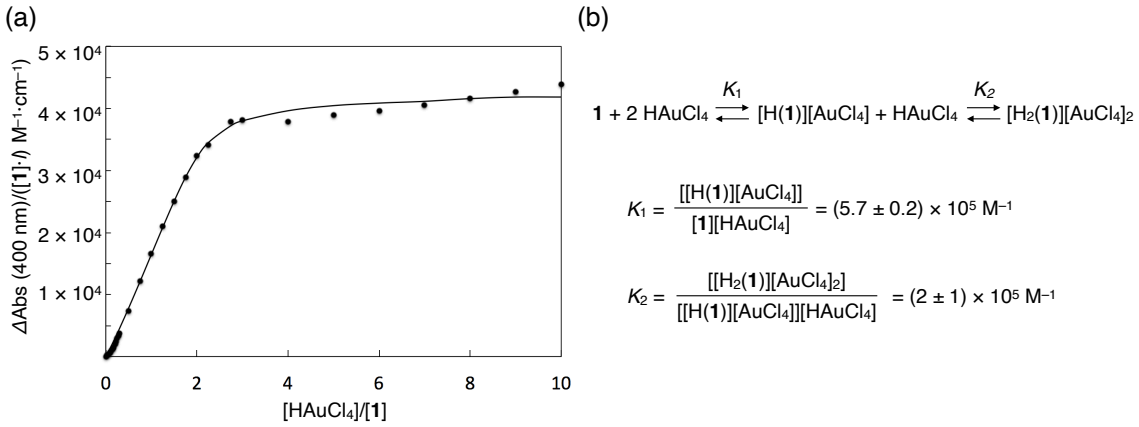

Figure 2–8. (a) Least-square fitting to the changes in absorbance ΔAbs at 400 nm (circle: observed; solid line: calculated) against molar ratio between $HAuCl_4$ and **1**; (b) definition and calculated values of apparent protonation constants K_1 and K_2. The curve fitting was conducted based on the theoretical absorption of species mentioned in the equation including free $HAuCl_4$. The mismatch of curve fitting with more than 2.25eq of $HAuCl_4 \cdot 4H_2O$ can be ascribed to the changes in the aggregation behaviors as mentioned below.

Aggregation behaviors of 1 and $HAuCl_4$

Effects of protonation on the aggregation behaviors of **1** in solution state were examined by dynamic light scattering (DLS) analysis. The measurement was conducted for samples with different molar ratios between **1** and $HAuCl_4$ in $CHCl_3/CH_3CN$ (10:1) to show formation of aggregate specific to the ratio: when 1.5 eq or 2.0 eq of $HAuCl_4 \cdot 4H_2O$ was mixed with **1**, signals for aggregate with hydrodynamic radius (*Z*-average) around 7-10 nm was observed (Figure 2-9). Since no such signals were detected with smaller amounts of $HAuCl_4$, it is obvious that addition of $HAuCl_4 \cdot 4H_2O$ triggered the aggregation. Furthermore, by addition of 3.0 eq of $HAuCl_4 \cdot 4H_2O$, *Z*-average became slightly larger and with much excess amount up to 5.0 eq, smaller *Z*-average (8.20 nm) and the size distribution (PdI, 0.204) were observed, indicating changes in the aggregation behaviors depending on the $[HAuCl_4]/[\mathbf{1}]$ ratio.

(a)

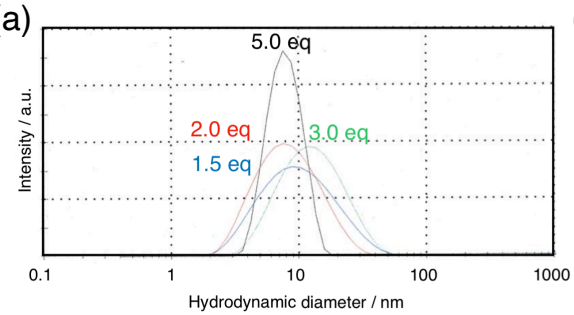

(b)

$[HAuCl_4]/[\mathbf{1}]$	Z-Average (nm)	PdI
≦ 1.0	Not detectable	
1.5	9.77	0.259
2.0	7.17	0.206
3.0	11.2	0.240
5.0	8.20	0.204

Figure 2–9. (a) DLS analysis of a $CHCl_3/CH_3CN$ (10:1) solution of **1** with different amounts of $HAuCl_4 \cdot 4H_2O$: (blue trace) $HAuCl_4 \cdot 4H_2O$ = 1.5 eq; (red trace) $HAuCl_4 \cdot 4H_2O$ = 2.0 eq; (green trace) $HAuCl_4 \cdot 4H_2O$ = 3.0 eq; (black trace) $HAuCl_4 \cdot 4H_2O$ = 5.0 eq; (b) hydrodynamic radius (*Z*-average) and polydispersity index (PdI) of each analysis.

Direct observation of the aggregates was performed by some microscopic measurements. Notably, AFM measurement of the solid sample prepared by spin-coating of a 1:2 mixture of **1** and $HAuCl_4 \cdot 4H_2O$ on mica plate showed fibrous aggregates (Figure 2-10c,d). The height of nanofibers was around 6 nm (Figure 2-10d) which showed good agreement with the maximum radius of **1** from the tip of one side chain to the other, indicating single-layer one-dimensional stacking the macrocycles (Figure 2-10i). The observation of small grains (Figure 2-10a,b) and different aggregation behaviors, entangled nanofibers with 3.0 eq of $HAuCl_4 \cdot 4H_2O$ (Figure 2-10e,f) and spherical aggregates with 5.0 eq of $HAuCl_4 \cdot 4H_2O$ (Figure 2-10g,f) also did not contradict the result of DLS analysis.[24] These results suggest that the protonation of two phenanthroline moieties of **1** with around 2.0 eq of $HAuCl_4 \cdot 4H_2O$ is a crucial factor for fiber formation.

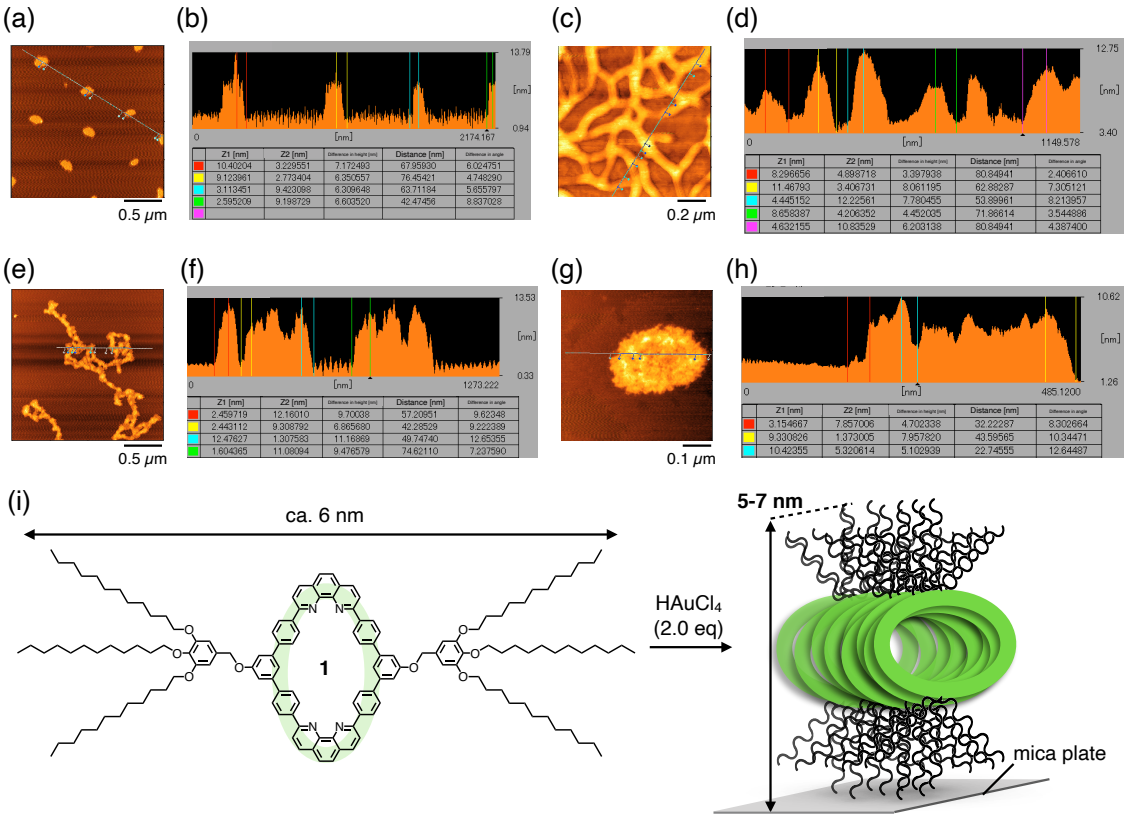

Figure 2–10. (a-e) AFM images and their cross sectional analyses along the line in the AFM images for the samples prepared by spin-coating of $CHCl_3/CH_3CN$ (10:1) solutions of **1** (102 μM) and different amount of $HAuCl_4$ on mica plates: (a,b) $HAuCl_4 \cdot 4H_2O$ = 0 eq; (c,d) $HAuCl_4 \cdot 4H_2O$ = 2.0 eq; (e,f) $HAuCl_4 \cdot 4H_2O$ = 3.0 eq; (g,h) $HAuCl_4 \cdot 4H_2O$ = 4.0 eq. (i) Schematic representation of the stacking mode of **1** within nanofibers observed in the AFM image with 2.0 eq of $HAuCl_4 \cdot 4H_2O$.

The composition of nanofibers was determined by STEM-EDS analysis. A dark-field STEM image showed submicron-sized nanofibers as observed in the AFM measurement (Figure 2-11a). The EDS analysis confirmed that the nanofibers included carbon atoms (Figure 2-11b) and gold atoms (Figure 2-11c) judging from the agreement between the elemental maps and STEM image. Since these atoms are derived from **1** and $HAuCl_4$, these results ensured that the nanofibers are composed of these substrates. On the other hand, PXRD pattern showed a tiny broadened signal assignable to the lattice plane around 1 nm distance (2θ = ca. 7), indicating a less regulated stacking structure of the two components (Figure 2-12).

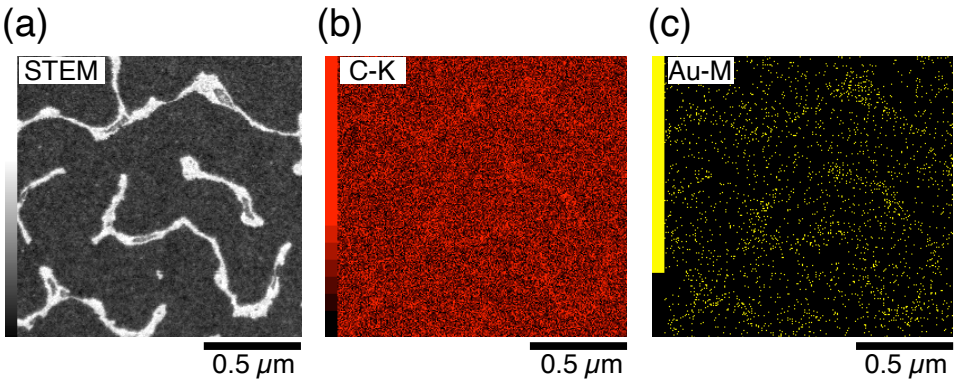

Figure 2–11. (a) A dark-field STEM image and (b,c) EDS maps: (b) C (K-peak); (c) Au (M-peak). The sample was prepared by drop-casting a 1:2 mixture of **1** and $HAuCl_4 \cdot 4H_2O$.

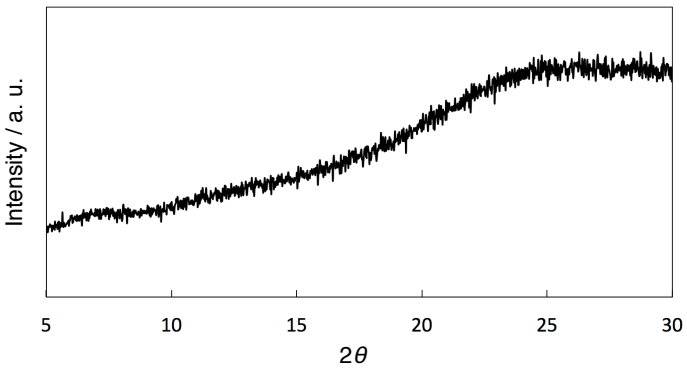

Figure 2–12. PXRD pattern of a solid sample prepared by air-drying a 1:2 mixture of **1** and $HAuCl_4 \cdot 4H_2O$.

Structural insight from partial compound [H(dpp)][$AuCl_4$]

More detailed insight of the supramolecular structure was obtained from single-crystal XRD analysis. Herein, a partial compound of **1**, 2,9-diphenyl-1,10-phenanthroline (dpp) was used instead due to the difficulty in crystallization of **1** with the long alkyl side chains. Analytical single crystals were obtained from a 1:1 mixture of dpp and $HAuCl_4 \cdot 4H_2O$ (Figure 2-13a). The crystal structure showed an ion-pair of cationic **1** with a proton at the nitrogen atom of the phenanthroline moiety and $AuCl_4^-$ anion (Figure 2-13b). These components formed alternating stacking by electrostatic interactions (N-H···Cl, N-Cl distance: 3.22 Å) and Au-π interactions (Au-π distance: 3.38 Å)[25] (Figure 2-13c). It is noteworthy that the electrostatic interactions between the two chloride atoms of $AuCl_4^-$ and protons of dpp are main factors for their one-dimensional bridging.

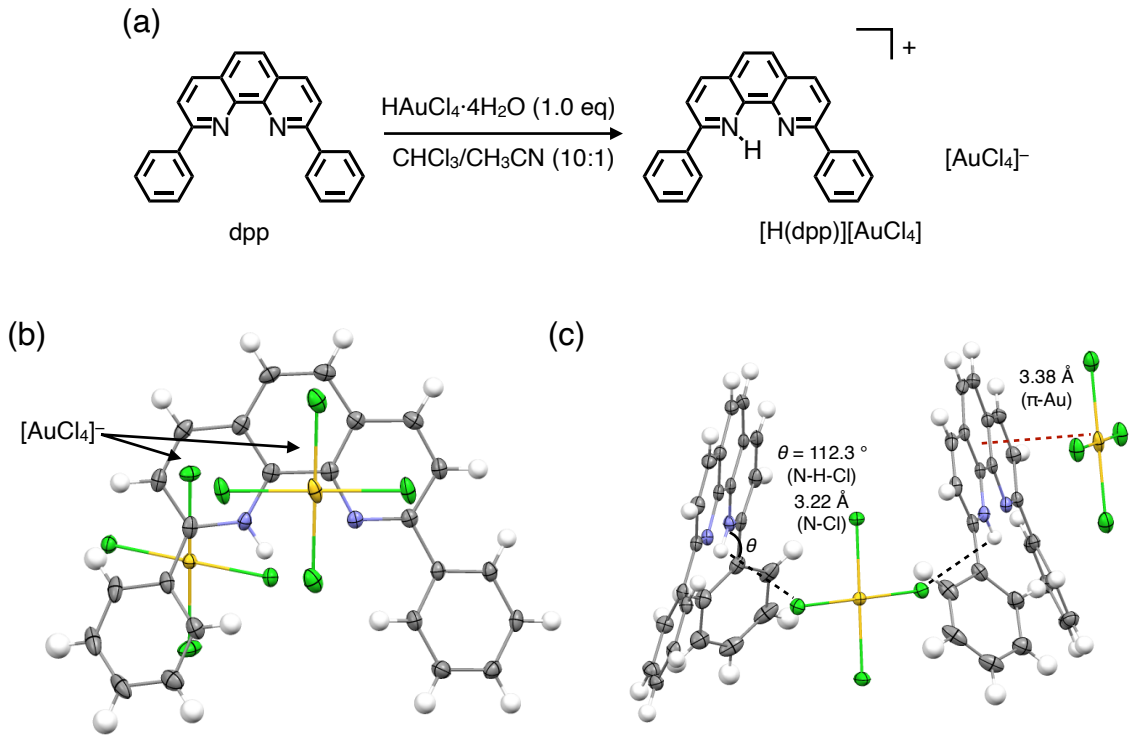

Figure 2–13. (a) Synthetic scheme of [H(dpp)][$AuCl_4$]; (b) crystal structure of [H(dpp)][$AuCl_4$] in ORTEP view (50% probability level); (c) stacking structure of [H(dpp)][$AuCl_4$] in the crystal structure (red dash line: Au-π interaction; black dash line: C-H···Cl interaction; Au: yellow, C: grey, Cl: light green, H: white, N: blue).

Considering all the experimental evidences, the fiber formation can be explained as follows: By addition of 2.0 eq of $HAuCl_4 \cdot 4H_2O$, the macrocycle **1** is doubly protonated at the two basic phenanthroline sites to generate the ion pair $[H_2(\mathbf{1})][AuCl_4]_2$. Then, the two protonated phenanthroline moieties are strongly bridged by $AuCl_4^-$ anions by multiple electrostatic interactions to form nanofibers arrayed with Au^{III} ions (Figure 2-14). From this consideration, the rigid macrocyclic motif with inward basic sites, which can restrict the direction of electrostatic interactions, seems to be the important motif for the anisotropic assembly.

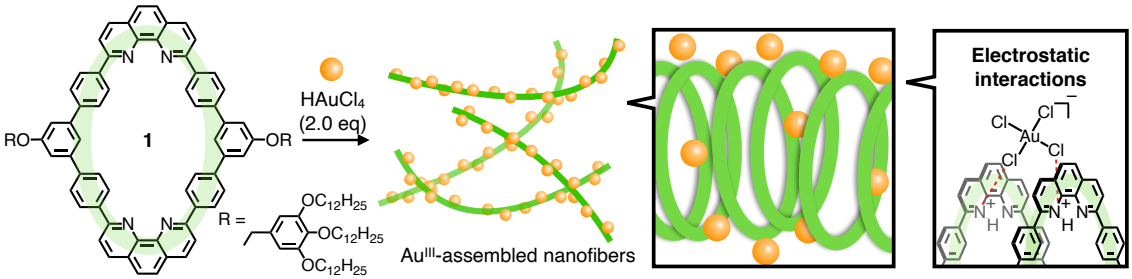

Figure 2–14. A plausible structure of Au^{III}-assembled nanofibers composed of protonated **1** and $[AuCl_4]^-$ by electrostatic interactions.

2–2–2. Pt^{IV}-assembled nanofiber

Since the investigation with $HAuCl_4$ ensured that protonation of **1** and electrostatic interaction is the main driving force for the fiber formation, construction of different metal-containing nanofibers was attempted by using other protic acid of anionic metal complexes to examine the applicability of this method. From this motivation, hexachloroplatinate acid, H_2PtCl_6, was used because hexachloroplatinate anion has a different charge number, size, and coordination geometry from tetrachloroauric acid.

First, the reaction of **1** and $H_2PtCl_6{\cdot}6H_2O$ was monitored by ^1H NMR measurement. The ^1H NMR showed gradual broadening of signals, which almost completed after addition of 1.0 eq of $H_2PtCl_6{\cdot}6H_2O$ (Figure 2-15). This result indicates double protonation of **1** and aggregation at this point as observed in the case with $HAuCl_4$.

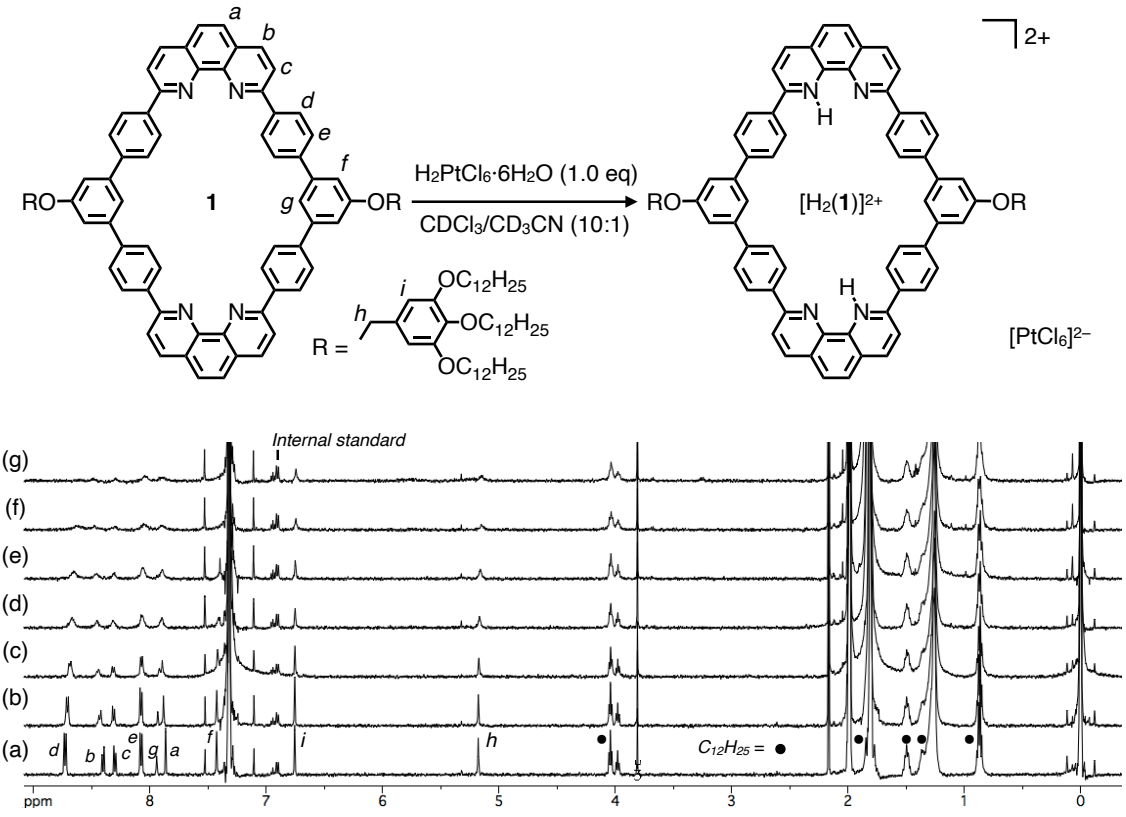

Figure 2–15. Partial ^1H NMR spectra (500 MHz, $CDCl_3/CD_3CN$ = 10/1, 300 K) of a mixture of **1** and different amounts of $H_2PtCl_6{\cdot}6H_2O$: (a) [**1**] = 84 μM, $H_2PtCl_6{\cdot}6H_2O$ = 0 eq; (b) $H_2PtCl_6{\cdot}6H_2O$ = 0.2 eq; (c) $H_2PtCl_6{\cdot}6H_2O$ = 0.4 eq; (d) $H_2PtCl_6{\cdot}6H_2O$ = 0.6 eq; (e) $H_2PtCl_6{\cdot}6H_2O$ = 0.8 eq; (f) $H_2PtCl_6{\cdot}6H_2O$ = 1.0 eq; (g) $H_2PtCl_6{\cdot}6H_2O$ = 1.2 eq. Anisole is included in the reaction mixture as an internal standard.

Aggregation behavior was investigated by AFM and STEM-EDS measurements. The AFM image clearly showed fiber formation by mixing **1** and $H_2PtCl_6 \cdot 6H_2O$ in a 1:1 ratio. The height of nanofiber was around 6-7 nm, which is almost comparable to the nanofibers with $HAuCl_4$, indicating the similar one-dimensional assembly of the macrocycle (Figure 2-16a, b). Notably, spherical aggregates were also observed with an excess amount of $H_2PtCl_6 \cdot 6H_2O$, which can be attributed to the existence of free H_2PtCl_6 to disturb the one-dimensional assembly (Figure 2-16c, d). STEM-EDS analysis showed good agreement between the fiber structure in the STEM image (Figure 2-16e) and the Pt map (Figure 2-16f) to confirm nanofibers arrayed with Pt^{IV} ions.

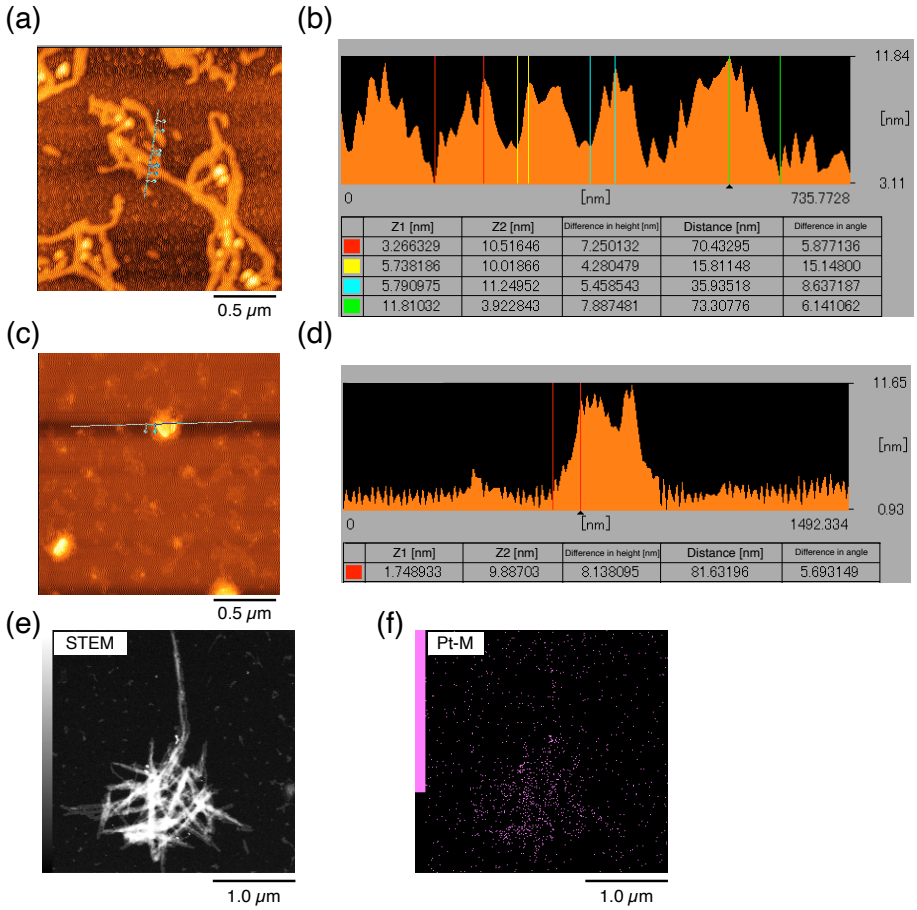

Figure 2–16. (a-d) AFM images and their cross sectional analyses along the line in the AFM images for the sample prepared by spin-coating of $CHCl_3/CH_3CN$ (10:1) solutions of **1** (102 μM) and different amount of $H_2PtCl_6 \cdot 6H_2O$ on mica plates: (a,b) $H_2PtCl_6 \cdot 6H_2O$ = 1.0 eq; (c,d) $H_2PtCl_6 \cdot 6H_2O$ = 2.0 eq. (e) A dark-field STEM image and (f) EDS map of Pt (M-peak). The sample for STEM-EDS analysis was prepared by drop-casting a 1:1 mixture of **1** and $H_2PtCl_6 \cdot 6H_2O$ on a carbon-coated Cu grid.

Crystallographic data were also obtained from a single crystal prepared by mixing partial compound dpp and $H_2PtCl_6 \cdot 6H_2O$ in a 1:0.5 molar ratio (Figure 2-17). Protonation at the phenanthroline site and ion-pair formation was confirmed by single-crystal XRD analysis (Figure 2-17a), resulting in the alternating one-dimensional stacking of $[H(dpp)]^+$ and $[PtCl_6]^{2-}$ by electrostatic interactions (N-H···Cl, N-Cl distance: 3.02 Å). From these results, it was revealed that H_2PtCl_6 can also be one-dimensionally assembled with macrocycle **1** in the same manner as $HAuCl_4$.

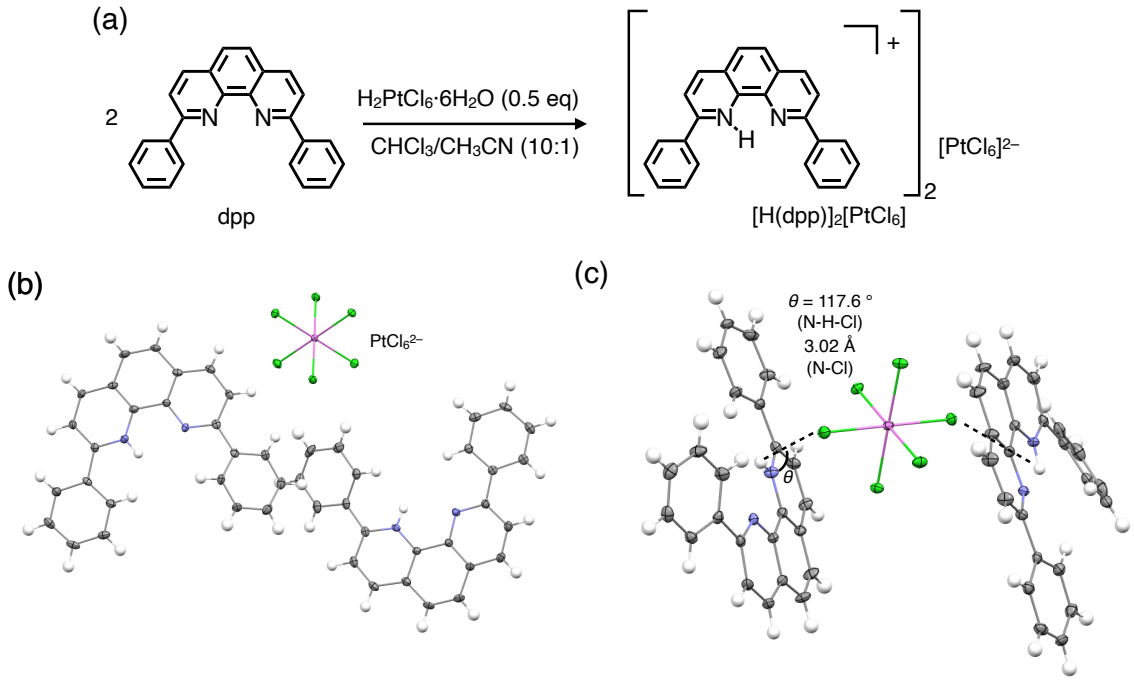

Figure 2–17. (a) Synthetic scheme of $[H(dpp)]_2[PtCl_6]$; (b) crystal structure of $[H(dpp)]_2[PtCl_6]$ in ORTEP view (50% probability level); (c) stacking structure of $[H(dpp)]_2[PtCl_6]$ in the crystal structure (black dash line: C-H···Cl interaction; C: grey, Cl: light green, H: white, N: blue, Pt: pink).

2–2–3. Mo^{VI}-assembled nanofibers

The applicability of protonation-induced one-dimensional assembly of metal ions was further investigated by using phosphomolybdate acid $H_3PMo_{12}O_{40}$ with a minus trivalent charge and a large molecular size (ca. 1 nm).

The reaction between **1** and $H_3PMo_{12}O_{40}\cdot nH_2O$ was monitored by ^1H NMR measurement. Upon addition of 0.7 eq of $H_3PMo_{12}O_{40}$, the spectrum showed significant broadening as seen in the other cases, indicating double protonation of **1** and aggregation (Figure 2-18).

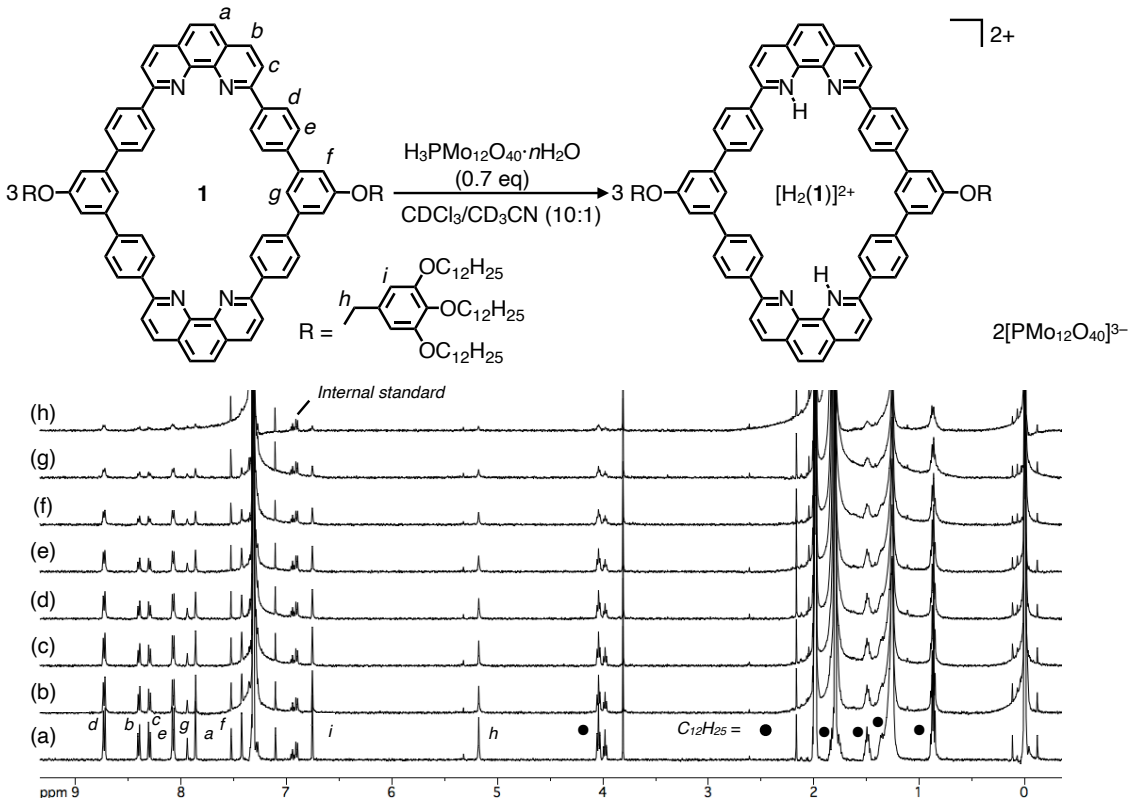

Figure 2–18. Partial ^1H NMR spectra (500 MHz, $CDCl_3/CD_3CN$ = 10/1, 300 K) of a mixture of **1** and different amounts of $H_3Mo_{12}O_{40}\cdot nH_2O$: (a) [**1**] = 96 μM, $H_3Mo_{12}O_{40}\cdot nH_2O$ = 0 eq; (b) $H_3Mo_{12}O_{40}\cdot nH_2O$ = 0.1 eq; (c) $H_3Mo_{12}O_{40}\cdot nH_2O$ = 0.2 eq; (d) $H_3Mo_{12}O_{40}\cdot nH_2O$ = 0.3 eq; (e) $H_3Mo_{12}O_{40}\cdot nH_2O$ = 0.4eq; (f) $H_3Mo_{12}O_{40}\cdot nH_2O$ = 0.5 eq; (g) $H_3Mo_{12}O_{40}\cdot nH_2O$ = 0.6 eq; (h) $H_3Mo_{12}O_{40}\cdot nH_2O$ = 0.7 eq. Anisole is included in the reaction mixture as an internal standard.

Nanofibers were also observed in AFM measurement from a 1:0.5 mixture of **1** and $H_3PMo_{12}O_{40}\cdot nH_2O$ (Figure 2-19a,b). The nanofibers showed regular height around 5-7 nm, indicating mono-layer one-dimensional assembly of macrocycle **1**. Changes into spherical aggregates were also observed with a 1:1 mixture of **1** and $H_3PMo_{12}O_{40}\cdot nH_2O$, which can be ascribed to the existence of free $H_3PMo_{12}O_{40}$ (Figure 2-19c,d). STEM-EDS analysis supported that the Mo atoms are aligned along the nanofibers judging from the agreement of the STEM image (Figure 2-19e) and the Mo map (Figure 2-19f).

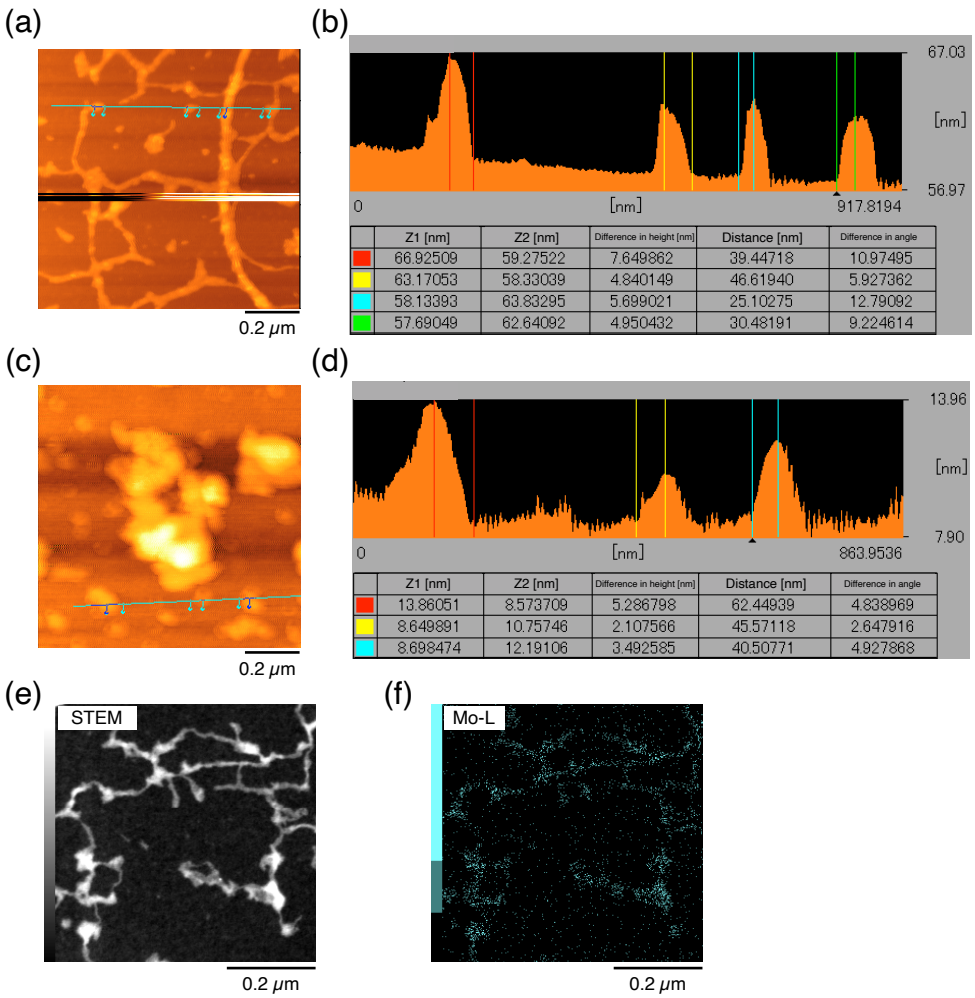

Figure 2–19. (a-d) AFM images and their cross sectional analyses along the line in the AFM images obtained by spin-coating of $CHCl_3/CH_3CN$ (10:1) solutions of **1** (102 μM) and different amounts of $H_3Mo_{12}O_{40}\cdot nH_2O$ on mica plates: (a,b) $H_3Mo_{12}O_{40}\cdot nH_2O$ = 0.5 eq; (c,d) $H_3Mo_{12}O_{40}\cdot nH_2O$ = 1.0 eq. (e) A dark-field STEM image and (f) EDS map of Mo (L-peak). The sample for STEM-EDS analysis was prepared by drop-casting a 1:0.5 mixture of **1** and $H_3Mo_{12}O_{40}\cdot nH_2O$ on a carbon-coated Cu grid.

A single crystal was also prepared from the partial compound dpp and $H_3PMo_{12}O_{40}\cdot nH_2O$ to conduct single-crystal XRD analysis (Figure 2-20a). Although $H_3PMo_{12}O_{40}$ was expected to react with 3 eq of dpp, the crystal structure showed the formation of 1:2 complex with one of the three protons located at DMF molecules (Figure 2-20b). The protonated dpp and $PMo_{12}O_{40}^{3-}$ showed one-dimensional stacking in the manner similar to $[H(dpp)]^+$ and $[PtCl_4]^-$, while $[H(dpp)]^+$ molecules are relatively apart from each other due to the large size of the $[PMo_{12}O_{40}]^{3-}$ anion which is stabilized by electrostatic interactions (N-H···O, N-O distance: 2.83 Å, Figure 2-20c). These results strongly suggest a wide applicability of this method for various metal ions with different size, charge number, and coordination geometry.

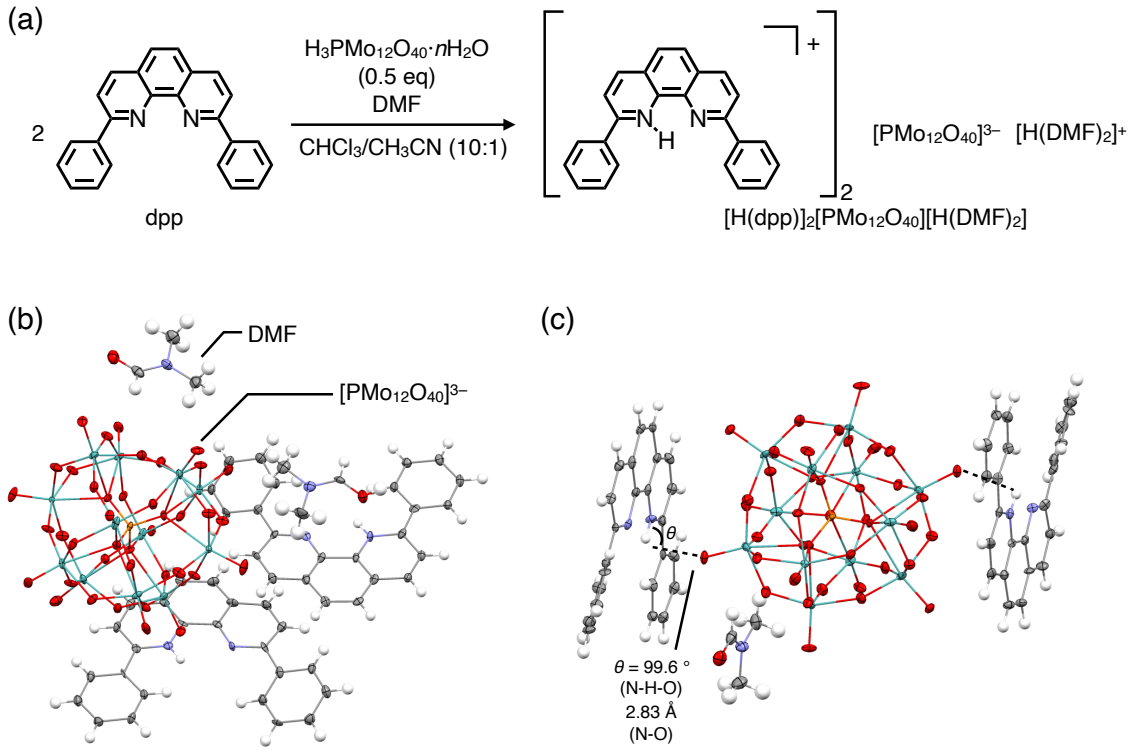

Figure 2–20. (a) Synthetic scheme of $[H(dpp)]_2[PMo_{12}O_{40}][H(DMF)_2]$; (b) crystal structure of $[H(dpp)]_2[PMo_{12}O_{40}][H(DMF)_2]$; in ORTEP view (50% probability level); (c) stacking structure of $[H(dpp)]_2[PMo_{12}O_{40}][H(DMF)_2]$ in the crystal structure (black dash line: C-H···O interaction; C: grey, H: white, Mo: light blue, N: blue, O: red).

2-3. Reduction of metal-assembled nanofibers

One of the attractive natures of metal ions is redox activity. As shown in Section 2-1, the redox properties of metal complexes are highly influenced by types, nuclear numbers, and arrangement of metal centers. Herein, the metal-assembled nanofibers were chemically reduced to afford unique reduced products.

2–3–1. Reduction of Au^{III}-assembled nanofibers into Au nanoparticles

Au nanoparticles have attracted much attention due to their structure-dependent photophysical properties and catalytic activities.[26] The size, property, and morphology of Au nanoparticles are highly dependent on the state before reduction.[27] Motivated by this fact, the Au^{III}-assembled nanofibers were subjected to reduction to synthesize Au nanoparticles. An excess amount of $NaBH_4$ (10 eq against **1**) was added to a $CHCl_3/CH_3CN$ solution of Au^{III}-assembled nanofibers ($[HAuCl_4]/[\mathbf{1}] = 2.0$) to reduce Au^{III} centers (Figure 2-21a). As a result, the color of the solution dramatically changed from yellow to purple which is derived from generated gold nanoparticles (Figure 2-21b). It is noteworthy that the resulting purple solid could be dispersed in $CHCl_3$, which showed sharp contrast to the precipitation of insoluble solid without **1** in a control experiment. The UV-vis spectrum of the product showed a broad absorption band around 533 nm, which could be assigned to the localized surface plasmon resonance of 10-20 nm-sized gold nanoparticles (Figure 2-21c).[28] The decrease in absorbance around 400 nm was also observed due to the possible neutralization of protonated **1**. The gold nanoparticles were directly observed by STEM measurement. The result revealed that the 10-30 nm-sized gold nanoparticles were existing near the nanofibers (Figure 2-21d,e), which is corresponding to the observation in UV-vis measurement. Consequently, preformation of Au^{III}-assembled nanofibers had some contribution to the size and dispersibility of the resulting gold nanoparticles.

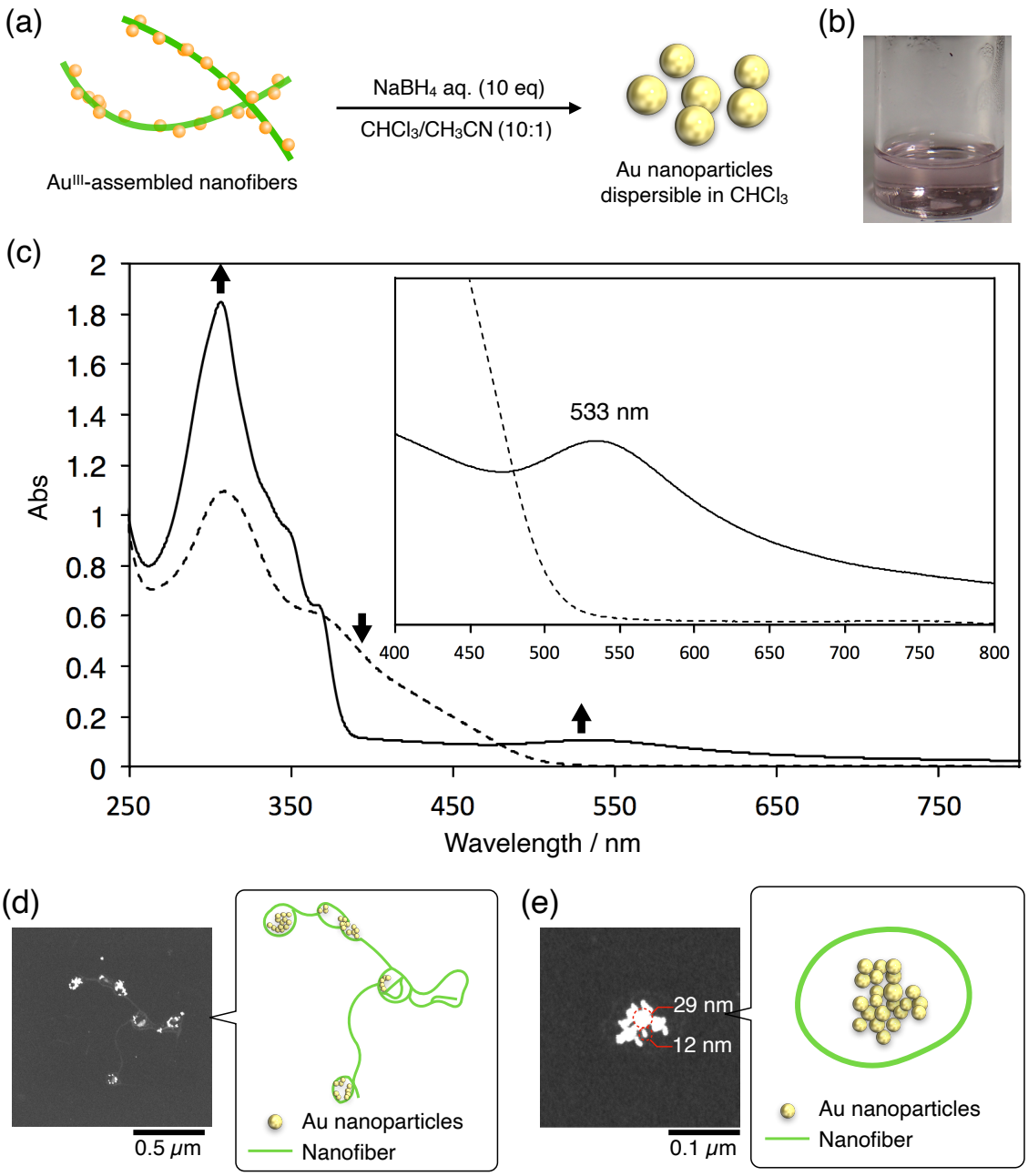

Figure 2–21. (a) Schematic representation of chemical reduction of the Au^{III}-assembled nanofibers. (b) Picture of the product dispersed in $CHCl_3$; (c) UV-vis absorption spectra of Au^{III}-assembled nanofibers before (dot line) and after (solid line) reduction ($CHCl_3$, 298 K). (d) STEM image of the obtained Au nanoparticles; (e) STEM image of the obtained Au nanoparticles in a narrow section. The samples for the STEM measurements were prepared by drop-casting a $CHCl_3$ solution on a carbon-coated Cu grid.

2–3–2. Reduction of Mo^{VI}-assembled nanofibers into Mo^{VI}/Mo^{V}-assembled mixed-valence nanofibers

Mo^{VI}-assembled nanofibers were also subjected to reduction by using L-ascorbic acid as a reductant (Figure 2-22a). After adding 3.0 eq of L-ascorbic acid to a 1:0.5 mixture of **1** and $H_3PMo_{12}O_{40}\cdot nH_2O$, a yellow solution gradually changed into a yellow-green solution (Figure 2-22b). UV-vis spectrum of this solution showed wide absorption band around 600-1200 nm region which can be attributed to inter-valence charge transfer between Mo^{V} and Mo^{VI} (Figure 2-22c). Of particular note is that the spectral change almost stopped with 3 eq of L-ascorbic acid. Since the molar ratio between L-ascorbic acid and the Mo atom is 6:1 at this point, assuming L-ascorbic acid as a two-electron donor, one of the twelve Mo centers in $H_3PMo_{12}O_{40}$ should be reduced to afford $[PMo_{12}O_{40}]^{4-}$ anions. During this process, increase in absorbance was not observed around 400 nm, indicating that macrocycle **1** retained protonated state. Notably, as shown in the AFM image, the fiber structure was also maintained after reduction (Figure 2-22d). Therefore, the Mo^{VI}-assembled nanofibers could be chemically reduced to Mo^{VI}/Mo^{V}-assembled mixed-valence nanofibers without deformation of the assembling structure.

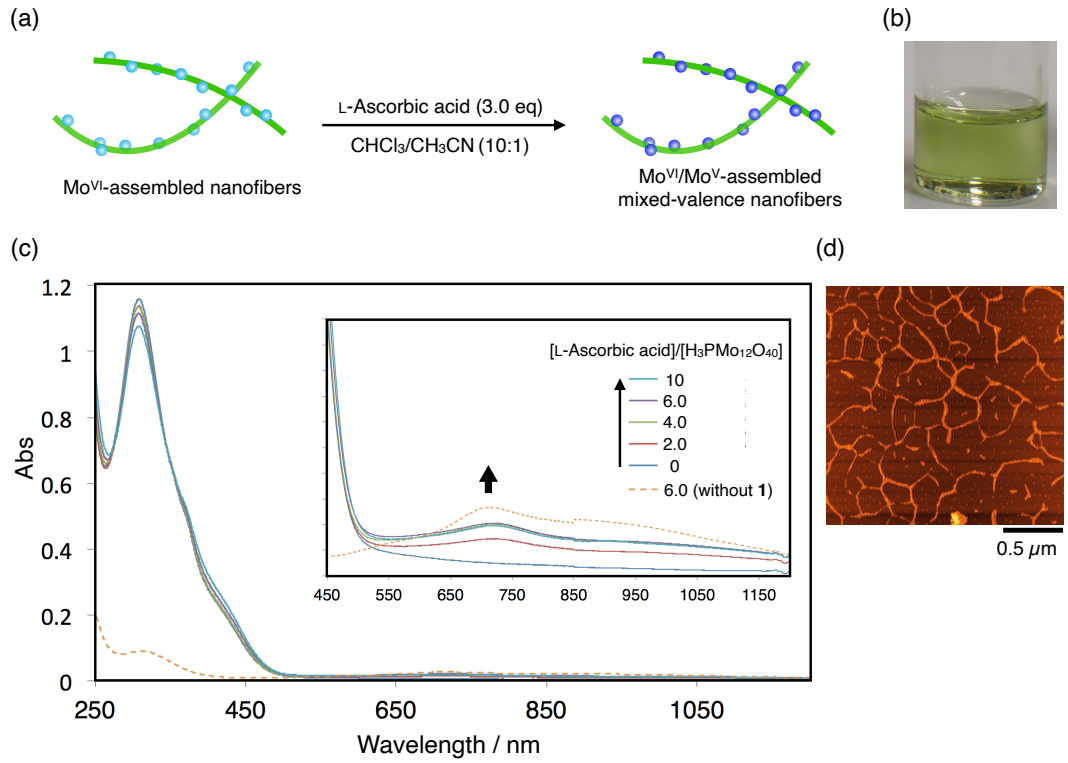

Figure 2–22. (a) Schematic representation of chemical reduction of the Mo^{VI}-assembled nanofibers. (b) Picture of the solution sample in $CHCl_3/CH_3CN$(10:1) after reduction by L-ascorbic acid. (c) UV-vis absorption spectra ($CHCl_3/CH_3CN$ = 10:1, 298 K) of Mo-assembled nanofibers reduced with different amounts of L-ascorbic acid (dot line: a mixture of $H_3PMo_{12}O_{40}$ and L-ascorbic acid in a 1:6 molar ratio). (d) AFM image of the nanofibers after reduction (spin-coated on mica).

2–4. Conclusions

In this chapter, I have developed a novel method for one-dimensional assembly of metal ions by utilizing a bisphenanthroline macrocycle **1**. It was revealed that protic acid of anionic metal complexes can trigger one-dimensional assembly of the macrocycle as confirmed by AFM and STEM measurements. The assembly mechanism was investigated to show that protonation of the two phenanthroline moieties of **1** is an important factor induce electrostatic interactions between cationic **1** with two protons and anionic metal complexes, resulting in formation of submicron-sized nanofibers with height of a single macrocycle. The wide applicability of this method was demonstrated by using various protic acids of anionic metal complexes such as $HAuCl_4$, H_2PtCl_6, and $H_3PMO_{12}O_{40}$ with different size, charge number and coordination geometry to synthesize Au^{III}-, Pt^{IV}-, and Mo^{VI}-assembled nanofibers.

Furthermore, reduction of the metal-assembled nanofibers was performed to synthesize unique materials. It was shown that Au^{III}-assembled nanofibers could be reduced to 10-30 nm-sized gold nanoparticles with high dispersibility in organic solvents. On the other hand, Mo^{VI}-assembled nanofibers could be partially reduced to Mo^{VI}/Mo^{V}-assembled mixed-valence nanofibers thanks to the low dependence of the assembly method on the state of metal centers. This research is expected to provide a scaffold for various one-dimensional metal arrangement, which will be useful for development of unique supramolecular materials.

2–5. Experimental

Macrocycle **1** and 2,9-diphenyl-1,10-phenanthroline (dpp) were synthesized according to literatures.[20] Chlorinated solvent $CHCl_3$ or $CDCl_3$ was treated with active basic alumina to exclude an effect by hydrogen chloride. Other solvents, organic and inorganic reagents, substrates are commercially available, and were used without further purification.

NMR spectroscopic measurement was performed using a Bruker AVANCE 500 spectrometer, and ^{1}H NMR spectra were calibrated based on the signal of $Si(CH_3)_4$ (0.00 ppm). UV-vis spectroscopy was conducted using a HITACHI U-3500 or a JASCO V-770 spectrophotometers. Atomic force microscope (AFM) images in dry-states were observed on an SII SPI4000 probe station with an SPA300HV unit using a DFM mode. Transmission electron microscope (TEM) images, scanning TEM (STEM) images and energy dispersive X-ray spectroscopy (EDS) mapping were obtained using a JEOL JEM-2100F microscope without staining. DLS measurements were performed using an OTSUKA ELECTRONICS DLS8000 instrument equipped with a He-Ne laser (633 nm wavelength). Electrospray ionization-time-of-flight (ESI-TOF) mass spectra were measured on a Waters LCT Premier XE spectrometer. Single-crystal X-ray diffraction (XRD) analyses were conducted using a Rigaku RAXIS-RAPID imaging plate diffractometer with MoKα radiation, and the obtained data were analyzed using a CrystalStructure crystallographic software package except for refinement, which was performed using SHELXL-2013 program suite.[29] X-ray structures were displayed using a Mercury program. Powder XRD analyses were performed using a Rigaku XtaLAB P200 diffractometer with CuKα radiation.

Au^{III}-assembled nanofibers

Concentration of **1** was determined by ^{1}H NMR measurement with anisole as an internal standard. Concentration of $HAuCl_4 \cdot 4H_2O$ was determined by UV-vis absorption measurement based on the reported extinction coefficient ($\varepsilon_{287(water)}$ = 3133 $L \cdot mol^{-1} \cdot cm^{-1}$).[30]

· ^{1}H NMR spectroscopic titration experiment and ESI-TOF analysis

A CD_3CN solution of $HAuCl_4 \cdot 4H_2O$ (1.81 mM) was added stepwise to a solution of **1** (84 μM, 1.0 mL, $CDCl_3/CD_3CN$ = 10/1, in the presence of 84 μM anisole as an internal standard), followed by ^{1}H NMR measurement. This operation was repeated until a total amount of the added $HAuCl_4$ reached 2.0 eq. The resultant 1:2 mixture of **1** and $HAuCl_4$ was also analyzed by ESI-TOF MS spectrometry.

· UV-vis titration experiment

A CH_3CN solution of $HAuCl_4 \cdot 4H_2O$ (2.90 mM) was added portionwise to a solution of **1** (29 μM, 4.0 mL, $CHCl_3/CH_3CN$ = 10/1), followed by UV-vis absorption measurement. This operation was repeated until a total amount of the added $HAuCl_4$ reached 10 eq. The errors of apparent protonation constants δK_1 and δK_2 were calculated from the cell length l and the initial concentration of the macrocycle $[\mathbf{1}]_0$ according to the following equation.

$$\delta K = \frac{1}{\sqrt{n}} \sqrt{\frac{1}{n-1} \sum_{i}^{n} \left(\frac{\partial K}{\partial [\mathbf{1}]} \frac{\partial [\mathbf{1}]}{\partial \Delta\varepsilon} + \frac{\partial K}{\partial [HAuCl_4]} \frac{\partial [HAuCl_4]}{\partial \Delta\varepsilon} \right)^2 (\delta \Delta\varepsilon)^2}$$

where:

$$\Delta\varepsilon = \frac{\Delta Abs}{[\mathbf{1}]_0 \cdot l}$$

· DLS analysis

A CH_3CN solution of $HAuCl_4 \cdot 4H_2O$ with different concentrations (22.9 mM, 26 μL, 1.0 eq; 34.4 mM, 26 μL, 1.5 eq; 45.8 mM, 26 μL, 2.0 eq; 68.7 mM, 26 μL, 3.0 eq; 115 mM, 26 μL, 5.0 eq) were added to a solution of **1** (120 μM, 5.0 mL) in $CHCl_3/CH_3CN$ (10/1), followed by DLS measurement.

· AFM measurement

A CH_3CN solution of $HAuCl_4 \cdot 4H_2O$ (1.81 mM, 56.4 μL, 2.0 eq; 2.72 mM, 56.4 μL, 3.0 eq; 3.62 mM, 56.4 μL, 4.0 eq) was added to a $CHCl_3$ solution of **1** (102 μM, 500 μL). Right after 10-fold dilution with $CHCl_3/CH_3CN$ (10/1), the mixture was spin-coated on mica to conduct AFM measurement.

· STEM-EDS measurement

A CH_3CN solution of $HAuCl_4 \cdot 4H_2O$ (2.07 mM, 100 μL, 1.9 eq) was added to a $CHCl_3$ solution of **1** (109 μM, 1.0 mL). Right after 3.3-fold dilution with $CHCl_3/CH_3CN$ (10/1), the solution was drop-cast on a carbon-coated Cu grid to conduct STEM and EDS measurement.

· PXRD measurement

A CH_3CN solution of $HAuCl_4 \cdot 4H_2O$ (1.88 mM, 530 μL, 2.0 eq) was added to a $CHCl_3$ solution of **1** (100 μM, 5.0 mL). The mixture was air-dried on a capillary glass tube to conduct powder X-ray diffraction analysis.

Reaction of dpp and $HAuCl_4 \cdot 4H_2O$

· Single-crystal XRD analysis

A $CHCl_3$ solution (300 μL) of dpp (2.3 mg, 6.8 μmol, 1.0 eq) and a CH_3CN solution (100 μL) of $HAuCl_4 \cdot 4H_2O$ (2.8 mg, 6.8 μmol, 1.0 eq) was mixed and filtrated, followed by Et_2O diffusion into the mixture for 1 day. The resulting yellow crystals were washed with EtOH (ca. 2 mL) and dried in *vacuo* to afford $[H(dpp)][AuCl_4]$ (3.8 mg, 5.6 μmol, 82%) as yellow needles. The structural data were deposited on the CCDC database (CCDC 2017589).

Crystal data for $[H(dpp)][AuCl_4]$: $C_{24}H_{17}Cl_4AuN_2$, $F_w = 672.19$, crystal dimensions 0.16 × 0.09 × 0.07 mm, monoclinic, space group $C2/c$, $a = 23.2563(7)$, $b = 8.9664(3)$, $c = 22.4002(7)$ Å, $\beta = 105.104(3)°$, $V = 4509.6(3)$ Å^3, $Z = 8$, $\rho_{calcd} = 1.980$ g cm^{-3}, $\mu = 7.036$ mm^{-1}, $T = 93$ K, λ(MoKα) = 0.71073 Å, $2\theta_{max} = 55.0°$, 17219/4984 reflections collected/unique ($R_{int} = 0.0204$), $R_1 = 0.0173$ ($I > 2\sigma(I)$), $wR_2 = 0.0409$ (for all data), GOF = 1.036, largest diff. peak and hole 1.51/–0.83 eÅ^{-3}. CCDC deposit number 2017589.

Pt^{IV}-assembled nanofibers

Concentration of $H_2PtCl_6 \cdot 6H_2O$ was determined by UV-vis absorption measurement based on the reported extinction coefficient ($\varepsilon_{259(water)}$ = ~24000 $L \cdot mol^{-1} \cdot cm^{-1}$).[31]

· ^1H NMR spectroscopic titration experiment and ESI-TOF analysis

A certain amount of a CH_3CN solution of $H_2PtCl_6 \cdot 6H_2O$ (200 μM) was measured out and dried in advance. The resulting solid was added to a solution of **1** (96 μM, 1.0 mL, $CDCl_3/CD_3CN$ = 10/1, in the presence of 84 μM anisole as an internal standard), followed by ^1H NMR measurement. This operation was repeated until a total amount of the added H_2PtCl_6 reached 1.2 eq.

· AFM measurement

A CH_3CN solution of $H_2PtCl_6 \cdot 6H_2O$ (2.03 mM, 21 μL, 1.0 eq; 1.72 mM, 21 μL, 2.0 eq) was added to a $CHCl_3$ solution of **1** (84 μM, 500 μL; 90 μM, 200 μL). Right after 10-fold dilution with $CHCl_3/CH_3CN$ (10/1), the mixture was spin-coated on mica to conduct AFM measurement.

· STEM-EDS measurement

A CH_3CN solution of $H_2PtCl_6 \cdot 6H_2O$ (1.72 mM, 18 μL, 1.0 eq) was added to a $CHCl_3$ solution of **1** (100 μM, 315 μL). Right after 10-fold dilution with $CHCl_3/CH_3CN$ (10/1), the solution was drop-cast on a carbon-coated Cu grid to conduct STEM and EDS measurement.

Reaction of dpp and $H_2PtCl_6 \cdot 6H_2O$

A $CHCl_3$ solution (300 μL) of dpp (2.7 mg, 8.1 μmol, 1.0 eq) and an EtOH solution (100 μL) of $H_2PtCl_6 \cdot 6H_2O$ (8.3 mg, 10.2 μmol, 1.3 eq) were slowly mixed for 3 days. The resulting yellow crystals were washed with CH_3CN (2 mL) and EtOH (1 mL), and then dried in *vacuo* to afford $[H(dpp)]_2[PtCl_6]$ (3.2 mg, 2.9 μmol, 73%) as yellow platelet crystals. The structural data were deposited on the CCDC database (CCDC 2017590).

Crystal data for $[H(dpp)]_2[PtCl_6]$: $C_{48}H_{34}Cl_6PtN_4$, F_w = 1074.63, crystal dimensions 0.18 × 0.08 × 0.07 mm, triclinic, space group $P\bar{1}$, a = 12.2029(2), b = 13.3559(2), c = 13.8683(2) Å, α = 80.7745(14), β = 67.0066(17), γ = 80.4839(16)°, V = 2040.61(6) $Å^3$, Z = 2, ρ_{calcd} = 1.749 g cm^{-3}, μ = 3.859 mm^{-1}, T = 93 K, λ(MoKα) = 0.71073 Å, $2\theta_{max}$ = 55.0°, 29499/9085 reflections collected/unique (R_{int} = 0.0411), R_1 = 0.0260 ($I > 2\sigma(I)$), wR_2 = 0.0544 (for all data), GOF = 1.035, largest diff. peak and hole 1.08/–1.05 e$Å^{-3}$. CCDC deposit number 2017590.

Mo^{VI}-assembled nanofibers

Concentration of **1** was determined by ^{1}H NMR measurement with anisole as an internal standard. Concentration of $H_3PMo_{12}O_{40}\cdot nH_2O$ was determined by UV-vis absorption measurement based on the reported extinction coefficient ($\varepsilon_{309.5(MeCN)}$ = 22300 L·mol^{-1}·cm^{-1}).[32]

· ^{1}H NMR spectroscopic titration experiment and ESI-TOF analysis

A certain amount of a CH_3CN solution of $H_3PMo_{12}O_{40}\cdot nH_2O$ (200 μM) was measured out and dried in advance. The resulting solid was added to a solution of **1** (96 μM, 1.0 mL, $CDCl_3/CD_3CN$ = 10/1, in the presence of 84 μM anisole as an internal standard), followed by ^{1}H NMR measurement. This operation was repeated until a total amount of the added H_2PtCl_6 reached 0.7 eq.

· AFM measurement

A CH_3CN solution of $H_3PMo_{12}O_{40}\cdot nH_2O$ (2.56 mM, 20 μL, 0.5 eq; 2.12 mM, 24 μL, 1.0 eq) was added to a $CHCl_3$ solution of **1** (100 μM, 1000 μL; 102 μM, 500 μL). Right after 10-fold dilution with $CHCl_3/CH_3CN$ (10/1), the mixture was spin-coated on mica to conduct AFM measurement.

· STEM-EDS measurement

A CH_3CN solution of $H_3PMo_{12}O_{40}\cdot nH_2O$ (536 μM, 100 μL, 5.0 eq) was added to a $CHCl_3$ solution of **1** (109 μM, 1.0 mL). Right after 10-fold dilution with $CHCl_3/CH_3CN$ (10/1), the solution was drop-cast on a carbon-coated Cu grid to conduct STEM and EDS measurement.

Reaction of dpp and $H_3PMo_{12}O_{40}\cdot nH_2O$

A $CHCl_3$ solution (400 μL) of dpp (1.0 mg, 3.1 μmol, 1.0 eq), DMF (100 μL) an CH_3CN solution (400 μL) of $H_3PMo_{12}O_{40}\cdot nH_2O$ (13.6 mg, 6.2 μmol, 2.0 eq, assumed n = 20) were slowly mixed with each other for 1 week. The resulting yellow crystals were washed with CH_3CN (2 mL) and EtOH (1 mL), and then dried in *vacuo* to afford $[H(dpp)]_2[PtCl_6]$ (3.2 mg, 2.9 μmol, 73%) as yellow platelet crystals. The structural data were deposited on the CCDC database (CCDC 2017591).

Crystal data for $[H(dpp)]_2[PMo_{12}O_{40}][H(DMF)_2]$: $C_{54}H_{49}Mo_{12}N_6O_{42}P$, F_w = 2636.24, crystal dimensions 0.440 × 0.230 × 0.180 mm, triclinic, space group $P1$, a = 12.24560(12), b = 12.33600(15), c = 13.69940(18) Å, α = 115.9800(12), β = 95.1937(9), γ = 102.8330(9)°, V = 1771.73(4) Å^3, Z = 1, ρ_{calcd} = 2.471 g cm^{-3}, μ = 2.172 mm^{-1}, T = 93 K, λ(MoKα) = 0.71073 Å, $2\theta_{max}$ = 55.0°, 43488/16131 reflections collected/unique (R_{int} = 0.0168), R_1 = 0.0329 ($I > 2\sigma(I)$), wR_2 = 0.0843 (for all data), GOF = 1.033, largest diff. peak and hole 2.14/–1.38 eÅ^{-3}, Flack parameter = 0.25(2). CCDC deposit number 2017591.

Reduction of Au^{III}-assembled nanofibers into Au nanoparticles

· Synthesis and UV-vis analysis

A CH_3CN solution of $HAuCl_4 \cdot 4H_2O$ (2.07 mM, 134 μL, 2.0 eq) was added to a $CHCl_3/CH_3CN$ (10:1) solution of **1** (139 μM, 1.0 mL, 1.0 eq). After stirring for 30 min, an aqueous solution of $NaBH_4$ (60 mM, 23 μL, 10 eq) was rapidly added to the reaction mixture under vigorous stirring. After stirring for 3 h, the purple organic layer was evaporated under reduced pressure to afford purple powder. The resulting solid was dissolved in $CHCl_3$ (1.0 mL), followed by UV-vis measurement.

· STEM-EDS analysis

Reduction of Au^{III}-assembled nanofibers was conducted in the procedure above using **1** (315 μM, 1.0 mL, 1.0 eq), $HAuCl_4 \cdot 4H_2O$ (19.3 mM, 33 μL, 2.0 eq), and $NaBH_4$ (82 mM, 38 μL, 10 eq). The resulting solid was dissolved in $CHCl_3/CH_3CN$ (10/1, 10 μM) and drop-cast on a carbon-coated Cu grid to conduct STEM and EDS analyses.

Reduction of Mo^{VI}-assembled nanofibers into Mo^{VI}/Mo^{V} mixed-valence nanofibers

· Synthesis, UV-vis and AFM analyses

An aqueous solution of L-ascorbic acid (356 μM, 270 μL, 3.0 eq) was measured out, and the solvent was removed under reduced pressure in advance. A mixture of **1** (82 μM, 1.7 eq) and $H_3PMo_{12}O_{40} \cdot nH_2O$ (49 μM) in $CHCl_3/CH_3CN$ (5.3:1, 660 μL) was added to the resulting solid. The mixture was allowed to stand at room temperature for 24 h in the dark, followed by UV-vis measurement. A mixture prepared in the same protocol was diluted to 10 μM with $CHCl_3/CH_3CN$ (10:1) and spin-coated on mica to conduct AFM measurement.

2–6. References

[1] Hui, J. K.-H.; MacLachlan, M. J. *Coord. Chem. Rev.* **2010**, *254*, 2363–2390.

[2] Marks, T. J. *Science* **1985**, *227*, 881–889.

[3] Cao, C.-S.; Shi, Y.; Xu, H.; Zhao, B. *Coord. Chem. Rev.* **2018**, *365*, 122–144.

[4] Oshio, H.; Nakano, M. *Chem. Soc. Rev.* **2011**, *40*, 3239–3248.

[5] Yam, V. W.-W.; Au, V. K.-M.; Leung, S. Y.-L. *Chem. Rev.* **2015**, *115*, 7589–7729.

[6] (a) Sakamoto, R.; Matsuoka, R.; Maeda, H.; Nishihara, H. *Chem. Soc. Rev*. **2015**, *44*, 7698–7714. (b) Nishimori, Y.; Kanaizuka, K.; Murata, M.; Nishihara, H. *Chem. Asian J*. **2007**, *2*, 367–376. (c) Maeda, H.; Sakamoto, R.; Nishihara, H. *Coord. Chem. Rev*. **2017**, *346*, 139–149.

[7] Ismayilov, R. H.; Wang, W.-Z.; Lee, G.-H.; Yeh, C.-Y.; Hua, S.-A.; Song, Y.; Rohmer, M.-M.; Benard, M.; Peng, S.-M. *Angew. Chem. Int. Ed*. **2011**, *50*, 2045–2048.

[8] Kajiwara, T.; Nakano, M.; Kaneko, Y.; Takaishi, S.; Ito, T.; Yamashita, M.; Igashira-Kamiyama, A.; Nojiri, H.; Ono, Y.; Kojima, N. *J. Am. Chem. Soc*. **2005**, *127*, 10150–10151.

[9] Po, C.; Anthony, Y.-Y. T.; Wong, K. M.-C.; Yam, V. W.-W. *J. Am. Chem. Soc*. **2011**, *133*, 12136–12146.

[10] (a) Hua, S.-A.; Cheng, M.-C.; Chen, C.-H. Peng, S.-M. *Eur. J. Inorg. Chem*. **2015**, 2510–2523. (b) Kondo, J.; Tada, Y.; Dairaku, T.; Hattori, Y.; Saneyoshi, H.; Ono, A.; Tanaka, Y. *Nat. Chem.* **2017**, *9*, 956–960. (c) Tanaka, K.; Tengaiji, A.; Kato, T.; Toyama, N.; Shionoya, M. *Science* **2003**, *299*, 1212–1213. (d) Tanaka, K.; Clever, G. H.; Takezawa, T.; Yamada, Y.; Kaul, C.; Shionoya, M.; Carell, T. *Nat. Nanotechnol*. **2006**, *1*, 190–194.

[11] (a) Nishimori, Y.; Kanaizuka, K.; Kurita, T.; Nagatsu, T.; Segawa, Y.; Toshimitsu, F.; Muratsugu, S.; Utsuno, M.; Kume, S.; Murata, M.; Nishihara, H. *Chem. Asian J*. **2009**, *4*, 1361–1367. (b) Leong, W. L.; Vittal, J. J. *Chem. Rev*. **2011**, *111*, 688–764.

[12] (a) Fukino, T.; Joo, H.; Hisada, Y.; Obana, M.; Yamagishi, H.; Hikima, T.; Takata, M.; Fujita, N.; Aida, T. *Science* **2015**, *344*, 499–504. (b) Schmidbaur, H.; Schier, A. *Angew. Chem. Int. Ed*. **2015**, *54*, 746–784. (c) Chan, M. H.-Y.; Leung, S. Y.-L.; Lam, W. H.; Yam, V. W.-W. *J. Am. Chem. Soc*. **2017**, *139*, 8639–8645.

[13] (a) Petitjean, A.; Cuccia, L. A.; Shcmutz, M.; Lehn, J.-M. *J. Org. Chem*. **2008**, *73*, 2581–2495. (b) Hui, J. K.-H.; Frischmann, P. D.; Tso, C.-H.; Michal, C. A.; MacLachlan, M. J. *Chem. Eur. J*. **2010**, *16*, 2453–2460. (c) Gallant, A. J.; MacLachlan, M. J. *Angew. Chem. Int. Ed.* **2003**, *42*, 5307–5310. (d) Davis, J. T. *Angew. Chem. Int. Ed*. **2004**, *43*, 668–698.

[14] (a) Wang, Z.; Medforth, C. J.; Shelnutt, J. A. *J. Am. Chem. Soc*. **2004**, *126*, 15954–15955. (b) Danjo, H.; Hirata, K.; Noda, M.; Uchiyama, S.; Fukui, K..; Kawahata, M.; Azumaya, I.; Yamaguchi, K.; Miyazawa, T. *J. Am. Chem. Soc*. **2010**, *132*, 15556–15558. (c) Yang, C.; Arvapally, P. K.; Tekarli, S. M.; Salazar, G. A.; Elbjeirami, O.; Wang, X.; Omary, M. A. *Angew. Chem. Int.*

Ed. **2015**, *54*, 4842–4846. (d) Liu, Z.; Fransconi, M.; Lei, J.; Brown, Z. J.; Zhu, Z.; Cao, D.; Lehl, J.; Liu, G.; Fahrenbach, A. C.; Botros, Y. Y.; Farha, O. K.; Hupp, J. T.; Mirkin, C. A.; Stoddart, J. F. *Nat. Commun.* **2013**, *4*, 1855.

[15] Horiuchi, S.; Tachibana, Y.; Yamashita, M.; Yamamoto, K.; Masai, K.; Takase, K.; Matsutani, T.; Kawamata, S.; Kurashige, Y.; Yanai, T.; Murahashi, T. *Nat. Commun.* **2015**, *6*, 6742.

[16] Kuroiwa, K..; Shibata, T.; Takada, A.; Nemoto, N.; Kimizuka, N. *J. Am. Chem. Soc*. **2004**, *126*, 2016–2021.

[17] Chen, C. Y.; Zeng, J. Y.; Lee, H. M. *In*org. *Chemie. Acta* **2007**, *360*, 21–30.

[18] Akine, S.; Utsuno, F.; Piao, S.; Orita, H.; Tsuzuki, S.; Nabeshima T., *Inorg. Chem*. **2016**, *55*, 810–821.

[19] Ren, C.; Maurizot, V.; Zhao, H.; Shen, J.; Zhou, F.; Ong, W. Q.; Du, Z.; Zhang, K.; Su, H.; Zeng, H. *J. Am. Chem. Soc*. **2011**, *133*, 13930–13933.

[20] Kuritani, M.; Tashiro, S.; Shionoya, M. *Chem. Asian J*. **2013**, *8*, 1368–1371.

[21] He, X.; Yam, V. W.-W. *Coord. Chem. Rev.* **2011**, *255*, 2111–2123.

[22] Wang, J.; Zhang, S.; Xu, C.; Wojtas, L.; Akhmedov, N. G.; Chen, H.; Shi, X. *Angew. Chem*. **2018**, *130*, 7031–7036.

[23] (a) Cesario, M.; Dietrich, C. O.; Edel, A.; Guilhem, J.; Kintzinger, J.-P.; Pascard, C.; Sauvage, J.-P. *J. Am. Chem. Soc*. **1986**, *108*, 6250–6254. (b) Armaroli, N.; De Cola, L.; Balzani, V.; Sauvage, J.-P.; Buchecker, C. O.; Kern, J.-M. *J. Chem. Soc. Faraday Trans.* **1992**, *88*, 553–556. (c) Listorti, A.; Esposti, A. D.; Kishore, R. S. K.; Kalsani, V.; Schmittel, M.; Armaroli, N. *J. Phys. Chem. A* **2007**, *111*, 7707–7718. (d) Accorsi, G.; Listorti, A.; Yoosaf, K.; Armaroli, N. *Chem. Soc. Rev*. **2009**, *38*, 1690–1700.

[24] Aliprandi, A.; Mauro, M.; De Cola, L. *Nat. Chem.* **2016**, *8*, 10–15.

[25] Tiekink, E. R. T.; Zukerman-Schpector, J. *CrystEngComm*. **2009**, *11*, 1176–1186

[26] (a) Dykman, L.; Khlebtsov, N. *Chem. Soc. Rev.* **2012**, *41*, 2256–2282. (b) Haume, K.; Rosa, S.; Grellet, S.; Smilek, M. A.; Butterworth, K. T.; Solov'yov, A. V.; Prise, K. M.; Golding, J.; Mason, N. J. *Cancer Nano* **2016**, *7*, 8. (c) Eustis, S.; El-Sayed, M. A. *Chem. Soc. Rev.* **2006**, *35*, 209–217. (d) Priyadarshini, E.; Pradhan, N. *Sensors and Actuators B* **2017**, *238*, 888–902.

[27] (a) Sengani, M.; Grumezescu, A. M.; Rajeswari, V. D. *OpenNano* **2017**, *2*, 37–46. (b) Li, N.; Zhao, P.; Astruc, D. *Angew. Chem. Int. Ed*. **2014**, *53*, 1756–1789.

[28] (a) Ahmadi, T. S.; Logunov, S. L.; El-Sayad, M. A. *J. Phys. Chem*. **1996**, *100*, 8053–8056. (b) Bellino, M. G.; Calvo, E. J.; Gordillo, G. *Phys. Chem. Chem. Phys*. **2004**, *6*, 424–428.

[29] Sheldric, G. M. *HELXL-97, Program for refinement of crystal structure* (University of Göttingen, Göttingen, Germany, 1997); SHELXL-2013 (University of Göttingen, Göttingen, Germany, 2013).

[30] Soni, V.; Sindal, R. S.; Mehrotra, R. N. *Inorg. Chemie. Acta* **2007**, *360*, 3141–3148.

[31] Holzner, G.; Kriel, F. H.; Priest, C. *Anal. Chem*. **2015**, *87*, 4757–4764.

[32] Nomiya, K.; Sugie, Y.; Amimoto, K.; Miwa, M. *Polyhedro*n **1987**, *6*, 519–524.

Chapter 3.

Kinetically Controlled Synthesis of Bisphenanthroline Macrocyclic Heterodinuclear metal complexes

本章については、５年以内に雑誌等で刊行予定のため、非公開。

Chapter 4.

Diastereoselective synthesis of chiral-at-bimetals macrocyclic heterodinuclear $Pt^{II}Cu^{I}$ complexes

本章については、５年以内に雑誌等で刊行予定のため、非公開。

Chapter 5.

Conclusions and perspectives

This study aimed at developing novel strategies for metal arrangement applicable to various metal ions by utilizing a bisphenanthroline macrocycle. For this purpose, one-dimensional assembly of various anionic metal complexes driven by protonation and electrostatic interactions, kinetically-controlled synthesis of heterodinuclear metal complexes, and diastereoselective synthesis of chiral-at-bimetals heterodinuclear complexes have been investigated.

In Chapter 2, I described a protonation-induced one-dimensional self-assembly of macrocycle **1** with anionic metal complexes driven by electrostatic interactions. Various protic acids of metal complexes such as $HAuCl_4$, H_2PtCl_6, and $H_3PMo_{12}O_{40}$ were used as a trigger for one-dimensional assembly. Protonation behaviors were studied by ^{1}H NMR spectroscopy, UV-vis spectroscopy, and ESI-MS spectrometry, and the aggregation behaviors were investigated both in solution state and in the solid state by DLS analysis, AFM measurement, and STEM-EDS measurement supported by single-crystal XRD analysis of partial compounds. As a result, it was confirmed that all the acids can induce diprotonation and one-dimensional assembly of **1** to afford micron-sized nanofibers arrayed with metal ions in a similar manner, which ensured the wide applicability of this method to various metal assembly processes. Furthermore, the obtained Au^{III}-assembled nanofibers could be reduced with $NaBH_4$ to give 10-30 nm-sized Au nanoparticles with high dispersibility in $CHCl_3$, meanwhile partial reduction of Mo^{VI}-assembled nanofibers with ascorbic acid afforded Mo^{VI}/Mo^{V} mixed-valence nanofibers (Figure 5-1a).

In Chapter 3, the syntheses of macrocyclic heterodinuclear metal complexes were conducted by sequential metal coordination in kinetic control. The first complexation was performed with Pt^{II} ion to obtain a kinetically stable mononuclear [PtCl(H$_{-1}$**1**)] complex. The kinetic stability allowed further metal coordination at the vacant phenanthroline coordination site with Zn^{II} or Cu^{I} ions to give a series of heterodinuclear metal complexes. In addition, metal-selective ligand exchange was carried out for the heterodinuclear $Pt^{II}Cu^{I}$ complex with a bulky dpp ligand to quantitatively afford an air-stable [PtCuCl(H$_{-1}$**1**)(dpp)](BF$_4$) complex (Figure 5-1b). The obtained complexes were fully characterized by ^{1}H NMR spectroscopy and ESI-MS spectrometry.

In Chapter 4, I succeeded in the syntheses of chiral-at-bimetals heterodinuclear metal complexes. By ligand exchange reaction of the C_s symmetric heterodinuclear $Pt^{II}Cu^{I}$ complex with a C_s symmetric 5-Ph-dpp ligand, a racemic mixture of (*R*)- and (*S*)-[PtCuCl(H$_{-1}$**1**)(5-Ph-dpp)](BF$_4$) chiral-at-bimetals complex was successfully obtained, whose kinetic stability was characterized by ^{1}H NMR spectroscopy. Moreover, bulkier ligand **2** afforded a single crystal of the corresponding chiral-at-bimetals complex, which was subjected to XRD analysis to show the distinctive diastereoselective formation of a racemic mixture of $(R)_{Cu}(R)_{Pt}$- and $(S)_{Cu}(S)_{Pt}$-[PtCuCl(H$_{-1}$**2**)(5-Ph-dpp)](BF$_4$) complexes (Figure 5-1c).

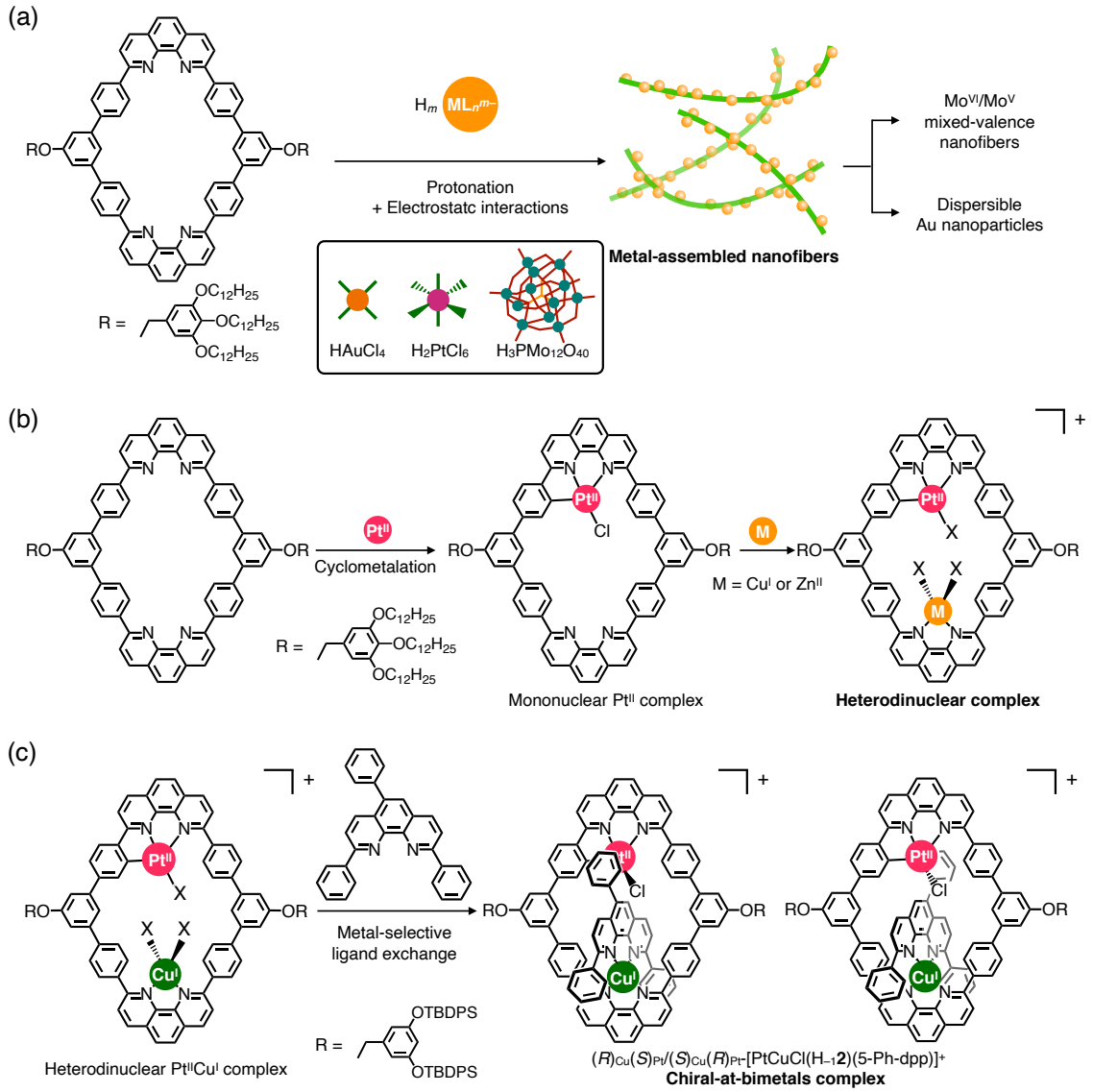

Figure 5–1. Three novel methods for metal arrangement with bisphenanthroline macrocyclic scaffolds developed in this study: (a) protonation-induced one-dimensional assembly of anionic metal complexes; (b) kinetically-controlled synthesis of heterodinuclear metal complexes; (c) diastereoselective synthesis of chiral-at-bimetals heterodinulear $Pt^{II}Cu^{I}$ complexes.

The first method, protonation-induced assembly, can be applied to other metal ions regardless of their coordination geometry to achieve various one-dimensional metal arrays which can lead to fundamental knowledge about one-dimensionally assembled metal ions and unique nanomaterials such as anisotropic metal clusters and electrical nanowires. On the other hand, the heterodinuclear metal complexes can exhibit heterometal-specific properties and functions. Especially, the chiral-at-bimetals $Pt^{II}Cu^{I}$ complex can be applied to chiroptical materials or asymmetric catalysts by utilizing the potentially emissive and catalytically active Pt^{II} center whose properties can be tuned by changing the structure of secondly incorporated ligand coordinating to the Cu^{I} center.

List of publications

[Publication related to the thesis]

1. Shohei Tashiro, Shun Shimizu, Masumi Kuritani, Mitsuhiko Shionoya, "Protonation-induced Self-assembly of Bis-phenanthroline Macrocycles into Nanofibers Arrayed with Tetrachloroaurate, Hexachloroplatinate or Phosphomolybdate Ions" *Dalton Trans*. **2020**, *49*, 13948-13953.

Acknowledgements

This research was conducted under the supervision of Professor Dr. Mitsuhiko Shionoya (The University of Tokyo) and Associate Professor Dr. Shohei Tashiro (The University of Tokyo). The DLS analysis in Chapter 2 was conducted in collaboration with Professor Dr. Eiichi Nakamura (The University of Tokyo) and Project Associate Professor Dr. Koji Harano (The University of Tokyo). The AFM analysis in Chapter 2 was conducted in collaboration with Professor Dr. Shin-ichi Ohkoshi (The University of Tokyo) and Assistant Professor Dr. Koji Nakabayashi (The University of Tokyo). The STEM-EDS analysis in Chapter 2 was conducted at the Advanced Characterization Nanotechnology Platform of the University of Tokyo, supported by the MEXT.

I deeply appreciate Professor Dr. Mitsuhiko Shionoya for the impressive and fruitful discussions and extraordinary care for my life as a researcher for 6 years.

I am strongly grateful to Associate Professor Dr. Shohei Tashiro (The University of Tokyo) for his kind technical and critical suggestions about research.

I am thankful to Assistant Professor Dr. Hitoshi Ube (The University of Tokyo) for his kind advices about organic syntheses and measurements.

I appreciate Assistant Professor Dr. Yusuke Takezawa (The University of Tokyo) for his smart ideas and concrete advices.

I gratefully acknowledge all the members of Shionoya laboratory to support my daily life in the laboratory. In particular, I would like to express my appreciation to Dr. Kenichiro Omoto for giving me fundamental research skills and valuable knowledge about the chemistry of macrocycles. I am also grateful to Dr. Masumi Kuritani, Mr. Tatsuya Kamatsuka, and Mr. Jugai Ou who enthusiastically studied the bisphenanthroline macrocycles.

I am thankful to Global Science Graduate Course (GSGC) program for the financial support and giving me an opportunity to interact with foreign students from different departments in English. I am also grateful for Professor Dr. Shin-ichi Ohkoshi (The University of Tokyo) to give me helpful advices as a vice supervisor.

Finally, I would like to express my sincere appreciation to my family for giving me heartful support for a long time.

Shun Shimizu